

High-throughput search for magnetic topological materials using spin-orbit spillage, machine-learning and experiments

Kamal Choudhary^{1,2}, Kevin F. Garrity¹, Nirmal J. Ghimire^{3,4}, Naween Anand⁵, Francesca Tavazza¹

¹ Materials Science and Engineering Division, National Institute of Standards and Technology, Gaithersburg, MD, 20899, USA.

² Theiss Research, La Jolla, CA 92037, USA.

³. Department of Physics and Astronomy, George Mason University, Fairfax, VA 22030, USA.

⁴. Quantum Science and Engineering Center, George Mason University, Fairfax, VA 22030, USA.

⁵. Materials Science Division, Argonne National Laboratory, Argonne, Illinois 60439, USA.

Abstract

Magnetic topological insulators and semi-metals have a variety of properties that make them attractive for applications including spintronics and quantum computation. We use systematic high-throughput density functional theory calculations to identify magnetic topological materials from the ≈ 40000 three-dimensional materials in the JARVIS-DFT database (<https://jarvis.nist.gov/jarvisdft>). First, we screen materials with net magnetic moment $> 0.5 \mu\text{B}$ and spin-orbit spillage > 0.25 , resulting in 25 insulating and 564 metallic candidates. The spillage acts as a signature of spin-orbit induced band-inversion. Then, we carry out calculations of Wannier charge centers, Chern numbers, anomalous Hall conductivities, surface bandstructures, and Fermi-surfaces to determine interesting topological characteristics of the screened compounds. We also train machine learning models for predicting the spillage, bandgaps, and magnetic moments of new compounds, to further accelerate the screening process. We experimentally synthesize and characterize a few candidate materials to support our theoretical predictions.

Corresponding author: kamal.choudhary@nist.gov

Introduction

The interplay of topology^{1,2} and electronic band structures in non-magnetic materials has led to several new material categories, most notably topological insulators (TI)^{1,3}, Dirac semi-metals, and broken-inversion Weyl semimetals (SM)^{4,5}, topological crystalline insulators⁶, nodal line semi-metals^{7,8}. However, many potentially useful quantum effects⁹⁻¹³, like anomalous Hall conductivity (AHC), are only possible in topological materials with broken time reversal symmetry (TRS), including exotic phases such as Chern insulators^{9,14}, magnetic axion insulators^{9,15}, and magnetic semimetals¹⁶. Experiments such as anomalous Hall conductivity¹⁷, spin-Seebeck¹⁸, spin-torque ferromagnetic resonance¹⁹, and angle-resolved photoemission spectroscopy (ARPES)²⁰, Fourier transform scanning tunneling spectroscopy (FT-STS)²¹, and Shubnikov de Haas (SdH) oscillations can be useful for analyzing the topological behavior. Only a few such materials are reported experimentally, and many of those materials are limited to very low temperatures or have trivial bands that overlap with the topological band features, limiting their utility. There is a significant opportunity to find more robust magnetic topological materials and to further our understanding of the underlying mechanisms leading to their topological properties.

A common feature of many topological materials classes is the presence of spin-orbit induced band inversion, where the inclusion of spin-orbit coupling in a calculation causes the character of the occupied wavefunctions at a k-point to change. Spin-orbit spillage (SOS)²²⁻²⁴ is a method to measure this band inversion by comparing the wavefunctions with and without spin-orbit coupling (SOC). SOS is based on density functional theory (DFT) calculations based wavefunction analysis and has been proven to be a useful technique for finding topological materials. Previous studies²²⁻²⁴ have looked at three-dimensional (3D) non-magnetic materials as well as two-dimensional (2D) materials with and without magnetism. Due to its ease of calculation, without any need for

symmetry analysis or dense k-point interpolation, the SOS is an excellent tool for identifying candidate materials to many topological phases. Advantages of the spillage technique include that it can apply to materials with low or no symmetries, including disordered or defective materials, and that it can identify the fundamental driver of topological behavior, the band inversion, even if the exact topological classification a material will depend on detailed features like the exact magnetic ordering, spin-direction, or sample thickness. After identifying high spillage materials, further analysis is necessary to identify the specific topological phases that may arise from the band inversion.

Stoichiometric magnetic topological insulators (MTIs) are very rare. MnBi_2Te_3 ^{25,26} , an antiferromagnetic TI, is one of the most studied and most well-characterized examples of a 3D MTI, and thin films of MnBi_2Te_3 exhibit quantized AHC. Several magnetic semimetals (MSM), such as CuMnAs , Fe_3GeTe_2 , LaCl , EuCd_2As_2 have been reported as well¹⁶. Recently there have been several efforts to systematically identify topological materials, especially for the non-magnetic systems^{23,24,27-29} . The spin orbit spillage technique has been successfully used to identify thousands of 3D non-magnetic insulators, semi-metals²³ as well as 2D non-magnetic and magnetic insulators and semimetals such as $\text{VAg}(\text{PSe}_3)_2$, ZrFeCl_6 , MnSe and TiCl_3 ²⁴. Identification of MTIs and MSMs has been developed by topological quantum chemistry groups^{30,31} in which wavefunction symmetry indicators are used to identify topological materials.

In this work, we screen for 3D magnetic topological insulators (MTI) and semimetals using the SOS technique. We then analyze the resulting high-spillage materials using conventional Wannier tight-binding Hamiltonian-based techniques to calculate Chern numbers, anomalous Hall conductivities, Berry-curvatures, and Fermi-surfaces, as well as to local band crossings. Starting with crystal structures optimized using the OptB88vdW³² van der Walls functional, we first

identify materials using the Perdew-Burke-Ernzerhof (PBE)³³ generalized gradient approximation (GGA) functional, and then carry out Strongly Constrained and Appropriately Normed (SCAN)³⁴ meta-GGA functional calculations of a subset of materials.

While our DFT-based computational screening is relatively efficient, it is still computationally expensive when applied to a set of thousands of materials. To further accelerate the identification and characterization process, we develop classification machine learning models for metals/non-metals, magnetic/non-magnetic and high-spillage/low-spillage materials, which acting together can screen topological materials in different classes. Specifically, we use JARVIS-ML based classical force-field inspired descriptors (CFID)³⁵ and gradient boosting decision tree (GBDT) for developing the ML models. CFID based models have been successfully been used for developing more than 25 high-accurate ML property prediction models³⁶. Using this approach, we can first predict topological materials using ML, then confirm with SOS and Wannier tight-binding approaches. The selected materials can be promising for experimental synthesis and characterizations. All the data and models generated through this work are publicly distributed through JARVIS-DFT^{23,24,36}, JARVIS-WTB³⁷ and JARVIS-ML webapps³⁶. We also share the computational tools and workflows developed for this work through JARVIS-Tools open access software to enhance the reproducibility and transparency of our work. As spillage is a computational screening technique for topological materials, there are many experimental techniques to delineate topological characteristics such as ARPES, SHE, and QHE. In this paper, we use some of these techniques to support the findings of spillage based two screened materials.

This paper is organized as follows: first we show the screening strategy for high-spillage magnetic materials and present statistical analysis of some of their properties. Next, we show bandstructures and k-point dependent spillage for a few example candidate materials to illustrate the strategy.

After that we further analyze selected insulating and metallic band structures with Wannier tight-binding approaches. Then, we analyze the periodic table distribution trends and develop machine learning classification models to accelerate the identification processes. Finally, we show experimental characterizations of a few candidate materials.

Results and discussion

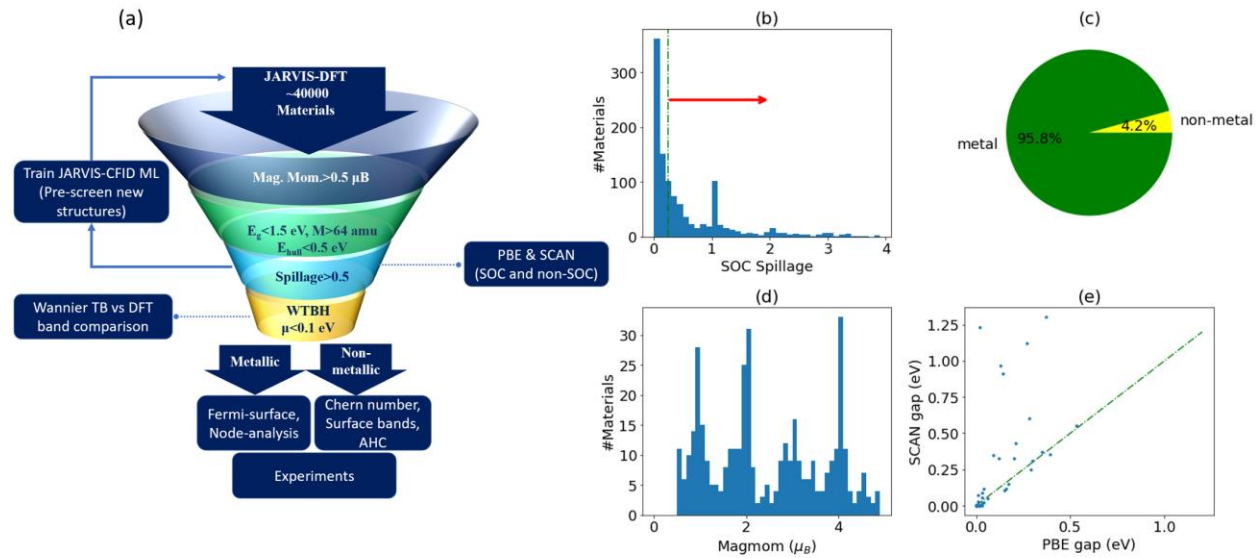


Fig. 1 Flow-chart for screening high-spillage materials and analysis. a) flowchart for screening, b) spillage distribution analysis for all the materials under investigation, c) pie chart showing high spillage insulators and metals, d) magnetic moment distribution for high-spillage materials, e) PBE vs SCAN bandgaps.

A flow chart for screening magnetic topological materials is shown in Fig. 1a. First, we screen for materials with net magnetic moment ($>0.5 \mu\text{B}$) in the ferromagnetic phase, which leads to 8651 candidates out of 39315 materials in the JARVIS-DFT database. Then we look for materials that are reasonably stable and are likely to display topological band inversion by screening for materials

that: a) are less than 0.5 eV/atom above the convex hull³⁸, b) have small bandgaps (<1.5 eV), and c) have at least one atom with high atomic mass (M>64). This results in 4734 remaining materials. We have computed the spin-orbit spillage (SOS) with PBE+SOC for 1745 materials (prioritizing the calculations of the number of atoms in unit cell less than 20). Next, we perform Wannier tight-binding Hamiltonian (WTBH) calculations with high quality (MaxDiff<0.1 eV)³⁷ to predict topological invariants, surface bandstructures, Fermi-surfaces, and anomalous Hall conductivity. So far, we have obtained high-quality WTBHs for 146 candidate materials. To study the effects of exchange-correlation, we run (SCAN)³⁴ meta-GGA functional calculations for high-spillage materials. Note that it may be difficult to carry out high dense k-point DFT calculations with SOC for thousands of materials, so after the WTBH generation, we carry our high-density k-point calculation Wannier TB models to find if the bandgap truly exists. Most of the materials studied in this work come from experimentally determined structures from the inorganic crystal structure database (ICSD) ³⁹.

In Fig. 1b we show the spillage distribution of the materials investigated in this work. As the spillage can be related to the number of band-inverted electrons at a k-point, we observe spikes at integer numbers²²⁻²⁴. Spin-orbit coupling can also change the mixing between different orbitals, rather than pure band inversion, which results in fractional spillage amounts. As shown in Fig. 1b using a spillage threshold of 0.25 for screening eliminates 51 % of materials, leaving 25 insulating and 564 metallic candidate materials with high spillage and non-zero magnetic moment. Similarly, in our previous works for 3D non-magnetic and 2D materials²²⁻²⁴, spillage technique was shown to discard more than 50 % candidates in the initial screening steps also. A material with non-zero spillage is a candidate topological material and we choose a threshold of 0.25 to narrow down the options. In Fig.1c we show the pie chart for high spillage insulating and metallic materials

distribution. This suggests that magnetic topological insulators (MTI) are far rare than semimetals. In the later sections, we discuss with examples some of the insulating and metallic high-spillage materials and characterize them using Wannier tight-binding Hamiltonian approach also. Next in Fig 1d, we observe that the magnetic moment of the systems could be up to $6 \mu\text{B}$ with mostly integer or close to integer values for the magnetic moments. For computational-expense reasons, in our initial screening, we only considered ferromagnetic spin configuration i.e., all spins of the system in a fixed direction. We expect that many of high-spillage materials that we find to be ferromagnetic may turn out to have lower energies in the anti-ferromagnetic or ferri-magnetic configurations. In Fig. 1e, we compare the bandgaps of the materials with PBE+SOC and SCAN+SOC for 65 high-spillage materials. Recently SCAN functional has been proposed as the functional to solve the bandgap and high correlated system issues which can be important for magnetic topological materials. SCAN has been shown to predict bandgaps and magnetic moments better than LDA, LDA+U, and PBE in many cases⁴⁰⁻⁴². We observe that SCAN+SOC bands are very close or in some cases slightly higher than PBE+SOC bandgaps for most of the materials. However, for some systems, it can be up to 10 times larger such as for LiVH_2OF_5 (JVASP-47705). Some of the materials which are metallic in PBE turns into insulating in SCAN predictions (for example, LiMnAsO_4 (JVASP-55805), $\text{Li}_4\text{Fe}_3\text{CoO}_8$ (JVASP-42538)), which indicates that the high spillage magnetic metals candidates can also be candidates for magnetic topological insulators. We provide more detailed PBE vs. SCAN comparisons in the supplementary information (Table S1).

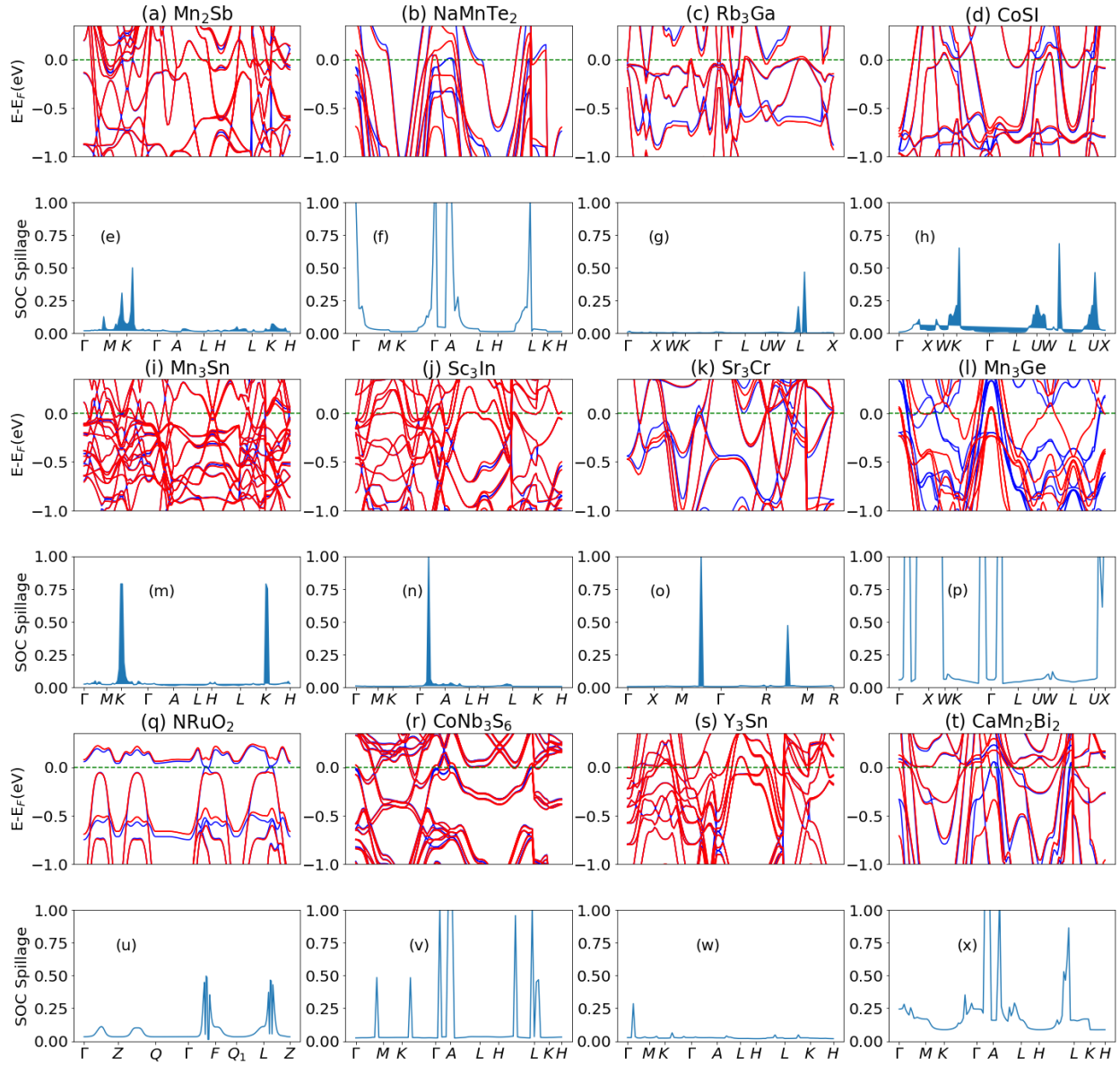


Fig. 2 Examples of bandstructure and k -dependent spin-orbit spillage plots for a few selected candidate materials with PBE+SOC. Bandstructures are shown in a) Mn_2Sb (JVASP-15693), b) NaMnTe_2 (JVASP-16806), c) Rb_3Ga (JVASP-38248), d) CoSI (JVASP-78508), i) Mn_3Sn (JVASP-18209), j) Sc_3In (JVASP-17472), k) Sr_3Cr (JVASP-37600), l) Mn_3Ge (JVASP-78840), q) NaRuO_2 (JVASP-8122), r) CoNb_3S_6 (JVASP-21459), s) Y_3Sn (JVASP-37701), t) CaMn_2Bi_2 (JVASP-18532). The red and blue lines show SOC and non-SOC bandstructures respectively. The k -dependent spillage is shown in (e), (f), (g), (h), (m), (n), (o), (p), (u), (v), (w) and (x) respectively.

In Fig. 2 we show the non-spin orbit and spin-orbit bandstructures for a few screened insulating and semi-metallic systems along with corresponding spin-orbit spillage plots such as a) Mn₂Sb (JVASP-15693), b) NaMnTe₂ (JVASP-16806), c) Rb₃Ga (JVASP-38248, d) CoSI (JVASP-78508), i) Mn₃Sn (JVASP-18209), j) Sc₃In (JVASP-17472), k) Sr₃Cr (JVASP-37600), l) Mn₃Ge (JVASP-78840), q) NaRuO₂ (JVASP-8122), r) CoNb₃S₆ (JVASP-21459), s) Y₃Sn (JVASP-37701), t) CaMnBi₂ (JVASP-18532). The red and blue lines show SOC and non-SOC bandstructures respectively. The k -dependent spillage is shown in (e), (f), (g), (h), (m), (n), (o), (p), (u), (v), (w) and (x) respectively. Such bandstructures and spillage plots for 11483 materials (including 2D and 3D magnetic and non-magnetic systems) are distributed through the JARVIS-DFT website along with several other materials properties such as crystal structure, heat of formation, elastic, piezoelectric, dielectric, and thermoelectric constants. In all of the cases the spillage is higher than 0.25 and the magnetic moments in the ferromagnetic configuration for these systems are more than 1 μ B. The NaRuO₂ shows a PBE+SOC gap of 56 meV while other materials are metallic. The insulating cases may also contain candidate Chern insulators as well as higher-order topological materials, and topological Mott insulators^{10,11}, which needs to be verified with detailed Wannier based calculations. An example analysis for NaRuO₂ is shown later. The semimetals contain Dirac and Weyl materials as well as several nodal line materials. An example analysis for nodal line Y₃Sn is shown below. We note that as we compare the wavefunctions from non-SOC and SOC calculations, there are chances that during turning on SOC the magnetic ordering can change compared to non-SOC case, which can give rise to spillage values unrelated to band inversion. Hence, it is important to further analyze the candidate materials with a more traditional technique such as Wannier tight-binding Hamiltonian (WTBH) generation and characterizations. In our earlier work³⁷, we have generated a large set of automated WTBH

database which we use here in this work to predict topological behavior and support our findings from the spillage calculations. The accuracy of WTBH is evaluated based on the MaxDiff criteria³⁷ which compares the maximum band-energy difference between DFT and WTB on k-points within and beyond our DFT calculations k-points. We set a MaxDiff (maximum energy difference at all k-points between Wannier and DFT bands) value of 0.1 eV as the tolerance for a good-quality WTBH. Out of all the spillage-based candidate materials we observe at least 146 high of them have low MaxDiff. For the systems with high spillage and high-quality WTBH, we predict Wannier charge centers, surface bandstructures, and anomalous Hall conductivity for the insulating cases and AHC, Fermi-surfaces and node plots for the metallic cases. Our Wannier database is available at <https://jarvis.nist.gov/jarviswtb/> with interactive features. We provide heat of formation, spacegroup, convex hull and other important details for each material in the corresponding webpage (such as <https://www.ctcms.nist.gov/~knc6/static/JARVIS-DFT/JVASP-8122.xml>) as well as in the supplementary information (Table S2) These webpages can also be downloaded as XML documents containing raw data for replotting or analysis by the users.

We identify NaRuO₂ as a candidate 3D Chern insulator through the above systematic screening process based on PBE+SOC and SCAN+SOC. NaRuO₂ is a trigonal system, belonging to R $\bar{3}m$ spacegroup. The heat of formation of the system is negative (-1.293 eV/atom) suggesting the system should be thermodynamically favorable. Also, the system has a formation energy that is 0.089 eV/atom above the convex hull, suggesting that the system is slightly unstable but in a range where it may be synthesizable, and it has in fact been synthesized experimentally⁴³. We observe that this material is metallic without SOC (Fig. 2a), but as we turn on SOC, a gap opens at the B and X points, which results in high spillage of 0.56. At least 18 materials show bandgap opening due to inclusion of spin-orbit coupling. Next, we calculate the Chern number and predict the

Wannier charge center. The Wannier charge center behavior is shown in Fig. 3a and b. As obvious we observe gapless charge centers which are key-features of the Chern insulators. The Chern number of four planes i.e., $k_1=0.0$; $k_1=0.5$; $k_2=0.0$; $k_2=0.5$ ($k_3=0.0$; $k_3=0.5$ and $k_2=0.0$; $k_2=0.5$ remaining the same); where k_1, k_2, k_3 is in fractional units is determined as -1. In Fig. 3c we see a conducting channel in the (001) surface suggesting that the material is conducting at its surface, but the bulk is insulating even though the time reversal is broken in the system. Chern number is directly proportional to the anomalous Hall conductivity which is an experimentally measured quantity. For a 3D Chern material, AHC is calculated as $\frac{C_3 b_3 e^2}{2\pi\hbar}$ which turns out to be $1540 \text{ ohm}^{-1}\text{cm}^{-1}$, which is what we find using Wannier calculation-based quantity in the Fig. 3d. In this case the AHC in Fig. 3d is quantized which can be leveraged for precise quantum control from the perspective of building devices. Using SCAN functional also, we find that the material to be semiconducting with a non-zero Chern number. The SCAN+SOC and PBE+SOC bandstructures for this material are shown in the supplementary information (Fig. S1), and are extremely similar.

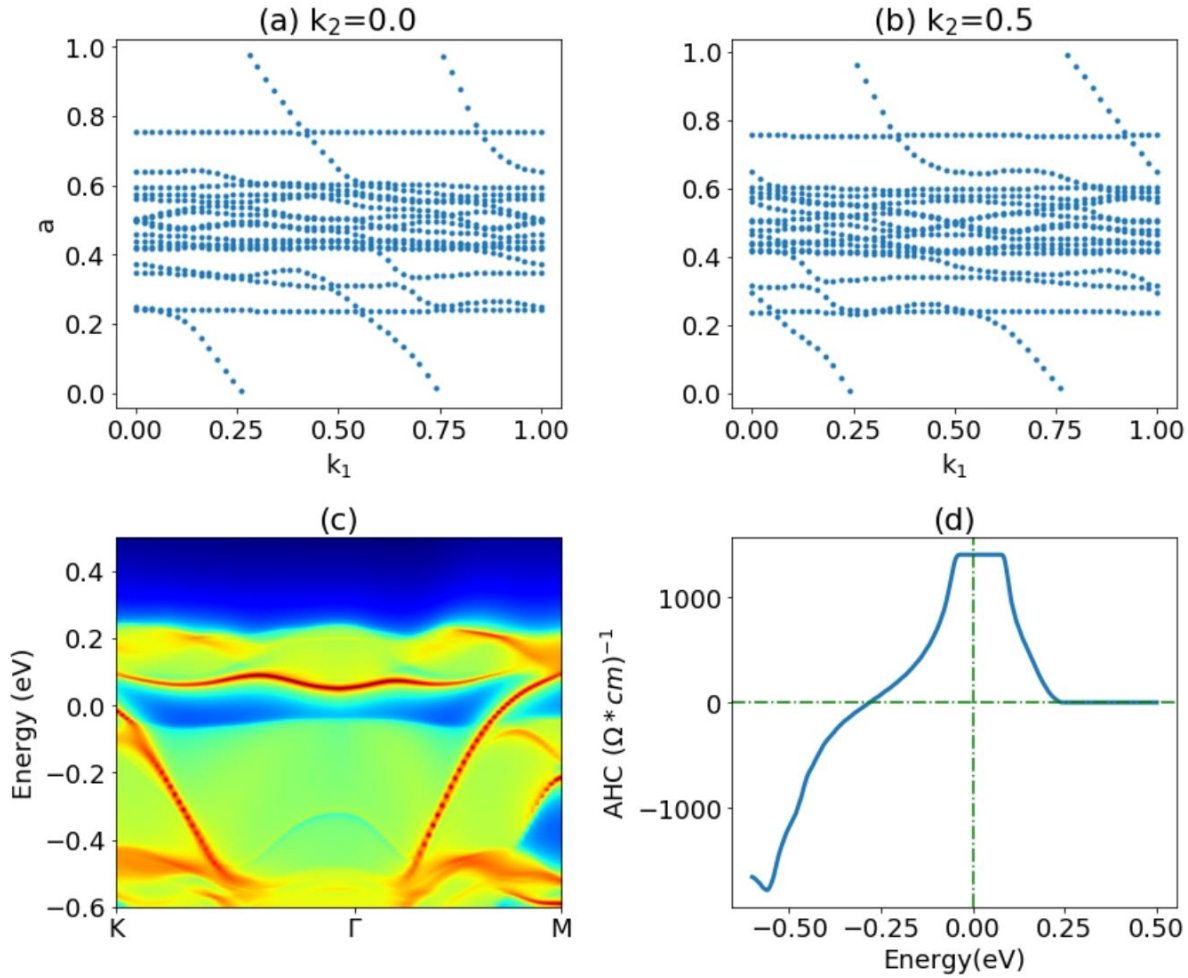


Fig. 3 Wannier-charge center, surface bandstructure and anomalous hall conductivity for $NaRuO_2$ (JVASP-8122) with PBE+SOC. a) Wannier charge centers (WCC) for $k_1=0.0$, b) $k_1=0.5$, c) (001) surface bandstructure, d) AHC plot for the compound.

In Fig. 4 we show the analysis of an example candidate topological metal Y_3Sn . Y_3Sn crystallizes in $P6_3mmc$ space group and hexagonal system, has negative formation energy (-0.43 eV/atom) and 0.1 eV/atom energy above convex hull, suggesting that it should be experimentally synthesizable. The bandstructures in Fig. 1w show multiple band crossings for this system and has a spillage of 0.25. We plot the Fermi surface of this system in Fig. 4a which shows several conducting Fermi-channels represented by deep blue spots. The lighter colors indicate that there are not bands at the

Fermi level. This material belongs to the Kagome lattice and such Fermi-surfaces have recently gained interest due to unique nodal line like features ^{44,45}. The (001) surface for this material also shows multiple bands crossing Fermi-level, which is shown in Fig. 4c. We observe several nodes in this material as shown in Fig. 4c with color coded energy level values. Energy levels with null value or blue color represents bands at Fermi level. The calculated anomalous Hall conductivity of this system is shown in Fig. 4d. The AHC is not quantized such as NaRuO_2 , but still has a non-zero value at zero field which can be due to the topological features of the bandstructure. The SCAN+SOC and PBE+SOC bandstructure comparison for this system is also shown in the supplementary section (Fig. S2), which shows shifts in energy for several bands.

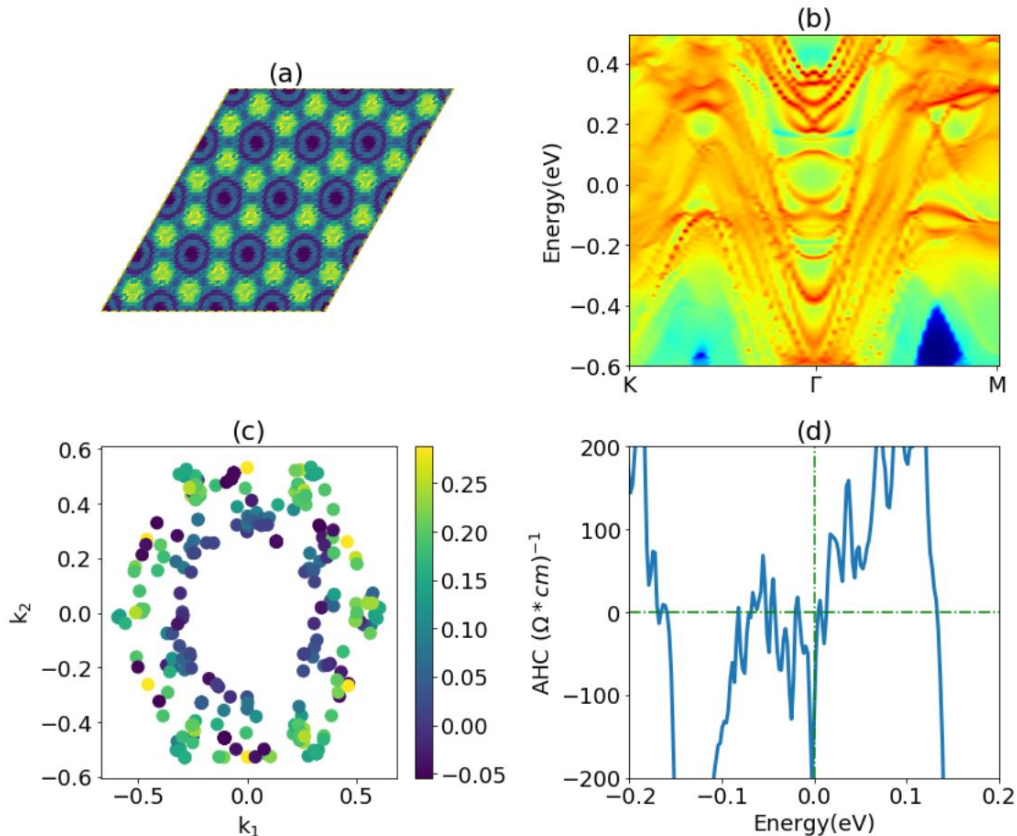


Fig. 4 Analysis for Y_3Sn (JVASP-37701) as a candidate semi-metal with PBE+SOC. a) Fermi-surface, b) (001) surface bandstructure, c) nodal points/lines, d) anomalous Hall conductivity.

Next, in Fig. 5a, we show the likelihood that a compound containing a given element has a high-spillage for the 4734 materials screened from step a. More specifically, for every compound containing a given element, we calculate the percentage that have a spillage greater than 0.25. Consistent with known TMs, we observe that materials containing the heavy elements such as Mn, Re, Fe, Ir, Pt, Bi and Pb are by far the likeliest ones to have high spillage. Other high spillage elements are the 5d elements. To contribute to SOC-induced band inversion, an element must both have significant SOC and contribute to bands located near the Fermi level, which favors heavy elements with moderate electronegativity. We use similar analysis for materials for thermoelectrics, solar cells, elastic constants etc. We can see some basic trends in the data but we intent to move towards more machine-learning perdition based on ML. To further accelerate the screening of magnetic topological materials we train three classification models using classical force-field inspired descriptors (CFID)³⁵ descriptors to predict the spillage, magnetic moment and bandgaps data in the JARVIS-DFT database. The CFID descriptors provide a complete set of structural chemical feature set (1557 for each material) which we use with Gradient Boosting Decision Tree (GBDT) algorithm as implemented in LightGBM⁴⁶ to train high accuracy ML models. The accuracy of the classification can be measured in terms of Receiver Operating Characteristic (ROC) Area Under Curve (AUC) which is 0.81 for spillage, 0.97 for both magnetic and for metallic models (using a 90 % to 10 % train test strategy). For a random guessing model, the ROC AUC is 0.5 while that for perfect model its 1.0. All of the models here have ROC AUC greater than 0.81 signifying high accuracy. Gradient boosting algorithm allows extracting feature importance after training the model. Some of the high-importance descriptors of the ML models are: unfilled *d*-orbitals, electronegativity which is intuitively reasonable. After training the ML models, we apply them on 1399770 materials from JARVIS, AFLOW⁴⁷, Materials-Project (MP)⁴⁸

and Open Quantum Materials Database (OQMD)⁴⁹ to find 77210 likely high-spillage materials using machine learning. The ML screened materials can then be subjected to the DFT workflow used in this work (see Fig. 1a) to further accelerate the search for magnetic topological materials. The ML models are distributed through the JARVIS-ML webapp.

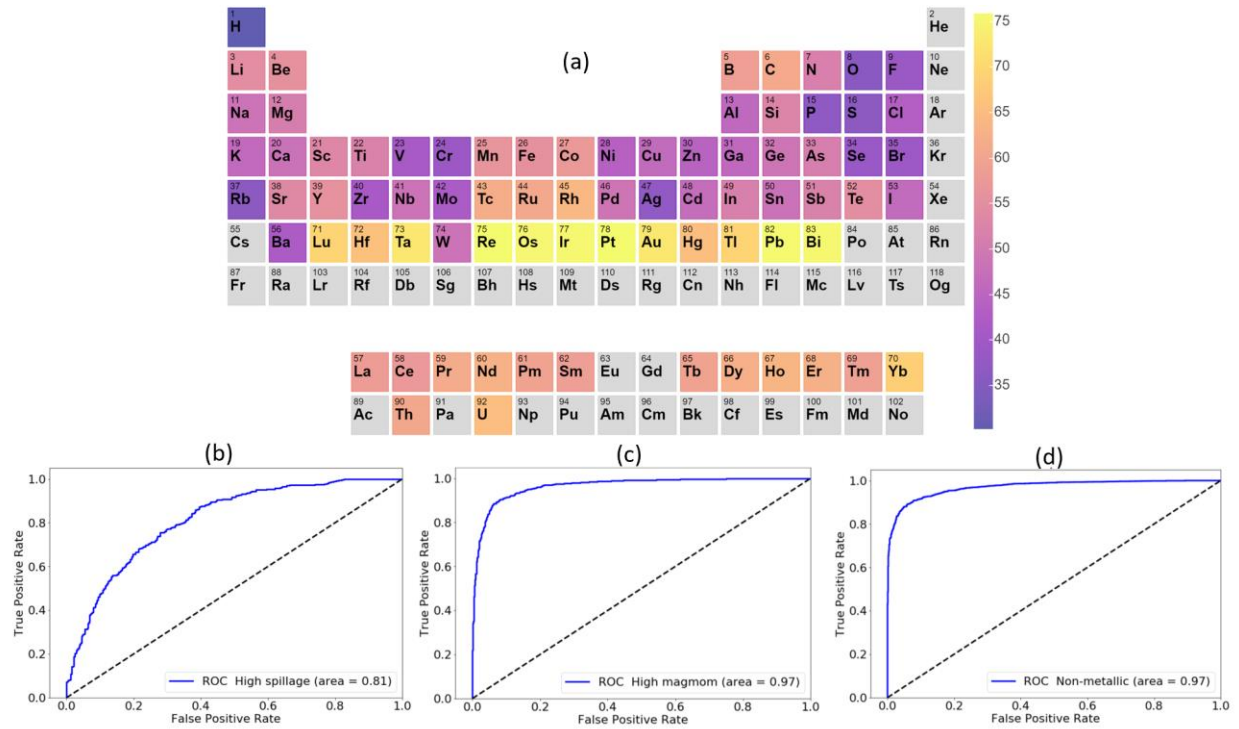


Fig. 5 Periodic table trends and classification model receiver operating characteristics (ROC) curves. a) periodic table trends of compounds with high-spillage values. The elements in a material are weighed 1 or 0 if the material has high or low-values. Then the percentage probability of finding the element in a high-value material is calculated. b) For high/low spillage model (threshold 0.25), c) high/low magnetic moment (threshold 0.5 μ B), d) Metals/non-metals based on electronic bandgaps (threshold 0.05 eV).

Next, we discuss experimental results that help us elucidate some of our theoretical findings. The Hall effect is an intrinsic property of a conductor due to the Lorentz force experienced by the

charge carriers. In systems with spontaneously broken time-reversal symmetry, an additional contribution, independent of the Lorentz force, is observed called anomalous Hall effect. The AHE was first observed in ferromagnets where its origin lies in the interplay between spin-orbit coupling (SOC) and magnetization. Berry phase calculations have been proven accurate to predict SOC-induced intrinsic AHE in ferromagnets including Weyl (semi)metals, non-collinear antiferromagnets, non-coplanar magnets, and other nontrivial spin textures. In Fig. 6a, we show the experimental anomalous Hall conductivity as a function of magnetic field at 23 K, 25 K and 23 K for CoNb_3S_6 . A large anomalous Hall conductivity at 23 K takes the value $27 \Omega^{-1} \text{ cm}^{-1}$, which is a signature of experimental non-trivial band topology. Corresponding computational non-SOC, SOC bandstructures for this system, which has a maximum spillage value of 0.5 are shown in Fig. 2t In Fig. 6b, we show the spin-pumping ferromagnetic resonance (SP-FMR) measurements by utilizing the inverse spin Hall effect (ISHE). In ISHE, a pure spin current \vec{J}_S gets converted to a charge current \vec{J}_C due to spin dependent asymmetric scattering phenomena. For spin pumping FMR measurements, $\text{Mn}_3\text{Ge}(100 \text{ nm})/\text{Py} (10 \text{ nm})$, $\text{Pt} (10 \text{ nm})/\text{Py} (10 \text{ nm})$ and $\text{Py} (10 \text{ nm})$ samples were prepared on sapphire substrate. A Pt device was also fabricated and analyzed because it provides an ideal benchmark for ISHE comparison. Fig. 6b shows the comparison between the ISHE charge current (V_{ISHE}/R_{eq}) for all three devices, where R_{eq} is the total device resistance across the contact pads. Resistance values R_{eq} for all devices were measured at room temperature in four-probe configuration. As expected, the Py single layer device is unaffected by ISHE, and thus V_{sp} is entirely antisymmetric. On the other hand, the peak V_{ISHE}/R_{eq} value of the $\text{Mn}_3\text{Ge}/\text{Py}$ device is significantly larger than that of the Pt/Py device. The ratio of spin-Hall angles $\theta_{SH}^{Mn3Ge}/\theta_{SH}^{Pt}$ is estimated to be around 8 ± 2 . The larger spin-Hall angle of Mn_3Ge is a result of non-trivial band-topology which is consistent with the spillage signature.

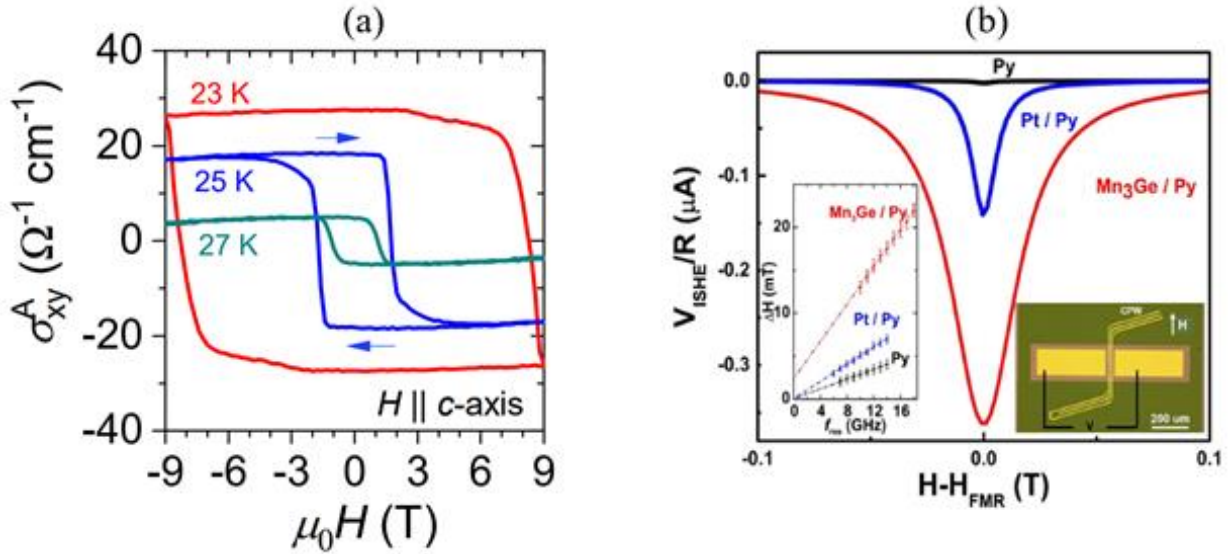


Fig. 6 Experimental measurements of some of the candidate materials. a) anomalous Hall effect of CoNb_3S_6 , b) comparison of inverse spin-Hall signal (symmetric component) among measured devices for Mn_3Ge . Right Inset: Optical image of the spin-pumping FMR device. Left Inset: Linear fit to the resonance linewidth (ΔH) at various resonance frequencies.

In summary, we have demonstrated the applicability of spin-orbit spillage, machine learning and experimental techniques to identify and characterize magnetic topological materials. We have also shown several remarkable trends in the topological chemistry with statistical analysis and periodic table distribution plots. We state the assumptions taken in this high-throughput approach such as neglecting magnetic transition temperature, magnetic ordering, dynamical stability, finding ground state for each material. Detailed investigation for each material is out of scope for this paper and will be taken in future. We have made our datasets and tools publicly available to enhance the reproducibility and transparency of our work. We believe our work can be of great help to experimental synthesis and characterization of such magnetic topological materials.

Methods

Density functional theory: DFT calculations were carried out using the Vienna Ab-initio simulation package (VASP)^{50,51} software using the workflow⁵⁹ given on our Github page (<https://github.com/usnistgov/jarvis>). We use the OptB88vdW functional³², which gives accurate lattice parameters for both vdW and non-vdW (3D-bulk) solids⁵². We optimize the crystal-structures of the bulk and monolayer phases using VASP with OptB88vdW. The initial screening step for <1.5 eV bandgap materials is done with OptB88vdW bandgaps from the JARVIS-DFT database. Because SOC is not currently implemented for OptB88vdW in VASP, we carry out spin-polarized PBE and spin-orbit PBE calculations in order to calculate the spillage for each material. Such an approach has been validated by Refs. ^{23,53}. The crystal structure was optimized until the forces on the ions were less than 0.01 eV/Å and energy less than 10^{-6} eV. We use Wannier90⁵⁴ and Wannier-tools⁵⁵ to perform the Wannier-based evaluation of topological invariants.

As introduced in Ref.⁵⁶, we calculate the spin-orbit spillage, $\eta(\mathbf{k})$, given by the following equation:

$$\eta(\mathbf{k}) = n_{occ}(\mathbf{k}) - \text{Tr}(P\tilde{P}) \quad (1)$$

where,

$P(\mathbf{k}) = \sum_{n=1}^{n_{occ}(\mathbf{k})} |\psi_{n\mathbf{k}}\rangle\langle\psi_{n\mathbf{k}}|$ is the projector onto the occupied wavefunctions without SOC, and \tilde{P} is the same projector with SOC for band n and k-point \mathbf{k} . We use a \mathbf{k} -dependent occupancy $n_{occ}(\mathbf{k})$ of the non-spin-orbit calculation so that we can treat metals, which have varying number of occupied electrons at each k-point²³. Here, ‘Tr’ denotes trace over the occupied bands. We can write the spillage equivalently as:

$$\eta(\mathbf{k}) = n_{occ}(\mathbf{k}) - \sum_{m,n=1}^{n_{occ}(\mathbf{k})} |M_{mn}(\mathbf{k})|^2 \quad (2)$$

where $M_{mn}(\mathbf{k}) = \langle \psi_{m\mathbf{k}} | \tilde{\psi}_{n\mathbf{k}} \rangle$ is the overlap between occupied Bloch functions with and without SOC at the same wave vector \mathbf{k} . If the SOC does not change the character of the occupied wavefunctions, the spillage will be near zero, while band inversion will result in a large spillage. After spillage calculations, we run Wannier based Chern and Z_2 -index calculations for these materials.

The Chern number, C is calculated over the Brillouin zone, BZ, as:

$$C = \frac{1}{2\pi} \sum_n \int d^2\mathbf{k} \Omega_n \quad (3)$$

$$\Omega_n(\mathbf{k}) = -\text{Im} \langle \nabla_{\mathbf{k}} u_{n\mathbf{k}} | \times | \nabla_{\mathbf{k}} u_{n\mathbf{k}} \rangle = \sum_{m \neq n} \frac{2\text{Im} \langle \psi_{n\mathbf{k}} | \hat{v}_x | \psi_{m\mathbf{k}} \rangle \langle \psi_{m\mathbf{k}} | \hat{v}_y | \psi_{n\mathbf{k}} \rangle}{(\omega_m - \omega_n)^2} \quad (4)$$

Here, Ω_n is the Berry curvature, $u_{n\mathbf{k}}$ being the periodic part of the Bloch wave in the n th band, $E_n = \hbar\omega_n$, v_x and v_y are velocity operators. The Berry curvature as a function of \mathbf{k} is given by:

$$\Omega(\mathbf{k}) = \sum_n \int f_{n\mathbf{k}} \Omega_n(\mathbf{k}) \quad (5)$$

Then, the intrinsic anomalous Hall conductivity (AHC) σ_{xy} is given by:

$$\sigma_{xy} = -\frac{e^2}{\hbar} \int \frac{d^3\mathbf{k}}{(2\pi)^3} \Omega(\mathbf{k}) \quad (6)$$

In addition to searching for gapped phases, we also search for Dirac and Weyl semimetals by numerically searching for band crossings between the highest occupied and lowest unoccupied band, using the algorithm from WannierTools⁵⁵. This search for crossings can be performed efficiently because it takes advantage of Wannier-based band interpolation. In an ideal case, the band crossings will be the only points at the Fermi level; however, in most cases, we find additional trivial metallic states at the Fermi level. The surface spectrum was calculated by using the Wannier functions and the iterative Green's function method^{57,58}.

Starting from ~40000 materials in the JARVIS-DFT database, we screened for materials with magnetic moment $>0.5 \mu\text{B}$ and having heavy elements (atomic weight ≥ 65) and bandgaps $<1.5 \text{ eV}$. After carrying out spin-orbit spillage calculations on them, we broadly classify them into insulators and semimetals with non-vanishing and vanishing electronic bandgaps. For materials with high spillage, we run Wannier calculations to calculate the Chern number, anomalous hall conductivity, surface bandstructures and Fermi-surfaces. We also run SCAN functional based calculations on the high spillage materials to check the changes in bandgaps and magnetic moments. So far, we have calculated 11483 SOSs for both magnetic/non-magnetic, metallic/non-metallic systems.

Machine learning model:

The machine-learning models are trained using classical force-field inspired descriptors (CFID) descriptors and supervise machine learning techniques using gradient boosting techniques in the LightGBM⁴⁶ package⁵⁹. The CFID gives a unique representation of a material using structural (such as radial, angle and dihedral distributions), chemical, and charge descriptors. The CFID provides 1557 descriptors for each material. We use ‘VarianceThreshold’ and ‘StandardScaler’ preprocessing techniques available in scikit-learn before applying the ML technique to remove low-variance descriptors and standardize the descriptor set. We use DFT data for developing machine learning models for high/low spillage (threshold 0.5), high/low magnetic moment (threshold $0.5 \mu\text{B}$), high/low bandgap (threshold 0.0 eV) to further accelerate the screening process

The CFID has been recently used to develop several high-accuracy ML models for material properties such as formation energies, bandgaps, refractive index, bulk and shear modulus and exfoliation energies k-points, cut-offs, and solar-cell efficiencies. The accuracy of the model is

evaluated based on area under curve (AUC) for the receiver operating characteristic (ROC). We provide a sample script for the ML training in the supplementary information.

Experimental details:

CoNb₃S₆:

Single crystals of CoNb₃S₆ were grown by chemical vapor transport using iodine as the transport agent⁵⁹. First, a polycrystalline sample was prepared by heating stoichiometric amounts of cobalt powder (Alfa Aesar 99.998 %), niobium powder (Johnson Matthey Electronics 99.8 %), and sulfur pieces (Alfa Aesar 99.9995 %) in an evacuated silica ampoule at 900 °C for 5 days. Subsequently, 2 g of the powder was loaded together with 0.5 g of iodine in a fused silica tube of 14 mm inner diameter. The tube was evacuated and sealed under vacuum. The ampoule of 11 cm length was loaded in a horizontal tube furnace in which the temperature of the hot zone was kept at 950 °C and that of the cold zone was ≈850 °C for 7 days. Several CoNb₃S₆ crystals formed with a distinct, well-faceted flat plate-like morphology. The crystals of CoNb₃S₆ were examined by single crystal X-ray diffraction at room temperature. Compositional analysis was done using an energy dispersive X-ray spectroscopy (EDS) at the Electron Microscopy Center, ANL.

Transport measurements were performed on a quantum design PPMS following a conventional 4-probe method. Au wires of 25 μm diameter were attached to the sample with Epotek H20E silver epoxy. An electric current of 1 mA was used for the transport measurements. The following method was adopted for the contact misalignment correction in Hall effect measurements. The Hall resistance was measured at H = 0 by decreasing the field from the positive magnetic field (RH+), where H represents the external magnetic field. Again, the Hall resistance was measured at H = 0 by increasing the field from negative magnetic field (RH-). Average of the absolute value

of (RH+) and (RH-) was then subtracted from the measured Hall resistance. The conventional antisymmetrization method was also used for the Hall resistance measured at 28 K (above TN) and at 2 K (where no anomalous Hall effect was observed), which gave same result as obtained from the former method.

Mn₃Ge:

In ISHE, a pure spin current \vec{J}_S gets converted to a charge current \vec{J}_C due to spin dependent asymmetric scattering phenomena⁵⁹. To maximize the ISHE signal, the external magnetic field is applied along [1 $\bar{1}$ 00] and dc voltage is measured along [11 $\bar{2}$ 0] directions. An optical image of the spin-pumping device is shown in Fig. 6b. For spin pumping FMR measurements, (i) Mn₃Ge (100 nm)/ Py (10 nm) and (ii) Pt (10 nm) Py (10 nm) (iii) Py (10 nm) samples were prepared on sapphire substrate. They were fabricated into 1000 μ m \times 200 μ m bars by photolithography and ion milling. Coplanar waveguides (CPW) with 170-nm thick Ti (20 nm)/Au (150 nm) were subsequently fabricated. Using ICP-CVD method, an additional SiN (150 nm) layer is deposited between CPW and the sample for electric isolation. The microwave frequencies were tuned between 10 GHz to 18 GHz with varying power (12 dBm - 18 dBm) while magnetic field was swept between -0.4 T to 0.4 T along the CPW axis. Measurements were performed at room temperature and field resolution of 2 mT was adopted throughout.

Data availability

JARVIS-related data is available at the JARVIS-API (<http://jarvis.nist.gov>), and JARVIS-DFT (<https://jarvis.nist.gov/jarvisdft/>) webpages.

Code availability

Python-language based codes with examples are available at JARVIS-tools page: <https://github.com/usnistgov/jarvis>.

Contributions

K.C. designed the computational workflows, carried out high-throughput calculations, analysis, and developed the websites. K.F.G helped in developing the workflow and analysis of the data. N.J.G. performed the experiments for CoNb₃S₆. N.A. performed the experiments for Mn₃Ge. All authors contributed to writing the manuscript.

References

- 1 Ortmann, F., Roche, S. & Valenzuela, S. O. *Topological insulators: Fundamentals and perspectives*. (John Wiley & Sons, 2015).
- 2 Vanderbilt, D. *Berry Phases in Electronic Structure Theory: Electric Polarization, Orbital Magnetization and Topological Insulators*. (Cambridge University Press, 2018).
- 3 Hasan, M. Z. & Kane, C. L. Colloquium: topological insulators. *Reviews of Modern Physics* **82**, 3045 (2010).
- 4 Novoselov, K. S. *et al.* Two-dimensional gas of massless Dirac fermions in graphene. *Nature* **438**, 197 (2005).
- 5 Huang, S.-M. *et al.* A Weyl Fermion semimetal with surface Fermi arcs in the transition metal monopnictide TaAs class. *Nature communications* **6**, 7373 (2015).
- 6 Fu, L. Topological crystalline insulators. *Physical Review Letters* **106**, 106802 (2011).
- 7 Bian, G. *et al.* Topological nodal-line fermions in spin-orbit metal PbTaSe 2. *Nature communications* **7**, 10556 (2016).
- 8 Burkov, A., Hook, M. & Balents, L. Topological nodal semimetals. *Physical Review B* **84**, 235126 (2011).
- 9 Varnava, N. & Vanderbilt, D. Surfaces of axion insulators. *Phys. Rev. B* **98**, 245117 (2018).
- 10 Raghu, S., Qi, X.-L., Honerkamp, C. & Zhang, S.-C. Topological mott insulators. *Phys. Rev. Lett.* **100**, 156401 (2008).
- 11 Schindler, F. *et al.* Higher-order topological insulators. *Science* **4**, eaat0346 (2018).
- 12 Zhou, Y., Kanoda, K. & Ng, T.-K. Quantum spin liquid states. *J. Rev. Mod. Phys.* **89**, 025003 (2017).
- 13 Sun, K., Yao, H., Fradkin, E. & Kivelson, S. A. Topological insulators and nematic phases from spontaneous symmetry breaking in 2D Fermi systems with a quadratic band crossing. *Phys. Rev. Lett.* **103**, 046811 (2009).
- 14 Thonhauser, T. & Vanderbilt, D. Insulator/Chern-insulator transition in the Haldane model. *Physical Review B* **74**, 235111 (2006).

15 Tokura, Y., Yasuda, K. & Tsukazaki, A. Magnetic topological insulators. *Nat Rev Phys* **1**, 126-143 (2019).

16 Zou, J., He, Z. & Xu, G. The study of magnetic topological semimetals by first principles calculations. *npj Comput. Mater.* *Nat Phys* **5**, 1-19 (2019).

17 Liu, E. *et al.* Giant anomalous Hall effect in a ferromagnetic kagome-lattice semimetal. *Nat Phys* **14**, 1125-1131 (2018).

18 Jiang, Z. *et al.* Enhanced spin Seebeck effect signal due to spin-momentum locked topological surface states. *Nat Comm.* **7**, 1-7 (2016).

19 Liu, L., Moriyama, T., Ralph, D. & Buhrman, R. Spin-torque ferromagnetic resonance induced by the spin Hall effect. *Phys. Rev. Lett.* **106**, 036601 (2011).

20 Lv, B., Qian, T. & Ding, H.. Angle-resolved photoemission spectroscopy and its application to topological materials. *Nat. Rev. Phys.* **1**, 609-626 (2019).

21 Simon, L., Bena, C., Vonau, F., Cranney, M. & Aubel, D. J. Fourier-transform scanning tunnelling spectroscopy: the possibility to obtain constant-energy maps and band dispersion using a local measurement. *J. Phys. D* **44**, 464010 (2011).

22 Liu, J. & Vanderbilt, D. Spin-orbit spillage as a measure of band inversion in insulators. *Physical Review B* **90**, 125133 (2014).

23 Choudhary, K., Garrity, K. F. & Tavazza, F. High-throughput Discovery of Topologically Non-trivial Materials using Spin-orbit Spillage. *Scientific Reports* **9**, 8534 (2019).

24 Choudhary, K. *et al.* Computational search for magnetic and non-magnetic 2D topological materials using unified spin-orbit spillage screening. *npj Computational Materials* **6**, 1-8 (2020).

25 Otrokov, M. M. *et al.* Prediction and observation of an antiferromagnetic topological insulator. *Nature* **576**, 416-422 (2019).

26 Li, J. *et al.* Intrinsic magnetic topological insulators in van der Waals layered MnBi₂Te₄-family materials. *Sci. Adv.* **5**, eaaw5685 (2019).

27 Vergniory, M. *et al.* A complete catalogue of high-quality topological materials. *Nature* **566**, 480-485 (2019).

28 Tang, F., Po, H. C., Vishwanath, A. & Wan, X. Comprehensive search for topological materials using symmetry indicators. *Nature* **566**, 486-489 (2019).

29 Bradlyn, B. *et al.* Topological quantum chemistry. *Nature* **547**, 298-305 (2017).

30 Xu, Y. *et al.* High-throughput calculations of magnetic topological materials. *Nature* **586**, 702-707 (2020).

31 Frey, N. C. *et al.* High-throughput search for magnetic and topological order in transition metal oxides. *Sci Adv* **6**, eabd1076 (2020).

32 Klimeš, J., Bowler, D. R. & Michaelides, A. Chemical accuracy for the van der Waals density functional. *J. Phys. Cond. Mat.* **22**, 022201 (2009).

33 Perdew, J. P., Burke, K. & Ernzerhof, M. Generalized gradient approximation made simple. *Phys. Rev. Lett.* **77**, 3865 (1996).

34 Sun, J., Ruzsinszky, A. & Perdew, Strongly constrained and appropriately normed semilocal density functional. *Phys. Rev. Lett.* **115**, 036402 (2015).

35 Choudhary, K., DeCost, B. & Tavazza, F. Machine learning with force-field-inspired descriptors for materials: Fast screening and mapping energy landscape. *Phys. Rev. Mater.* **2**, 083801 (2018).

36 Choudhary, K. *et al.* The joint automated repository for various integrated simulations (JARVIS) for data-driven materials design. *npj Computational Materials* **6**, 1-13 (2020).

37 Garrity, K. F. & Choudhary, K. Database of Wannier Tight-binding Hamiltonians using High-throughput Density Functional Theory. *arXiv:2007.01205* (2020).

38 De Jong, M. *et al.* Charting the complete elastic properties of inorganic crystalline compounds. *Sci Data* **2**, 1-13 (2015).

39 Kane, C. L. & Mele, E. J. Quantum spin Hall effect in graphene. *Phys. Rev. Lett.* **95**, 226801 (2005).

40 Tran, F. *et al.* Semilocal exchange-correlation potentials for solid-state calculations: Current status and future directions. *J. App.Phys.* **126**, 110902 (2019).

41 Nokelainen, J. *et al.* Ab initio description of the $\text{Bi}_2\text{Sr}_2\text{CaCu}_2\text{O}_{8+\delta}$ electronic structure. *Phys. Rev. B* **101**, 214523 (2020).

42 Zhang, Y., Sun, J., Perdew, J. P. & Wu, X. Comparative first-principles studies of prototypical ferroelectric materials by LDA, GGA, and SCAN meta-GGA. *Phys. Rev. B* **96**, 035143 (2017).

43 Shikano, M., Delmas, C. & Darriet, J. NaRuO_2 and $\text{Na}_x\text{RuO}_2 \gamma \text{H}_2\text{O}$: New Oxide and Oxyhydrate with Two Dimensional RuO_2 Layers. *J. Inorg. Che.* **43**, 1214-1216 (2004).

44 Ali, M. N. *et al.* Butterfly magnetoresistance, quasi-2D Dirac Fermi surface and topological phase transition in ZrSiS . *Sci Adv* **2**, e1601742 (2016).

45 Müller, C. *et al.* Determination of the Fermi surface and field-induced quasiparticle tunneling around the Dirac nodal loop in ZrSiS . *Phys. Rev. Res.* **2**, 023217 (2020).

46 Ke, G. *et al.* in *Advances in neural information processing systems*. 3146-3154.

47 Curtarolo, S. *et al.* AFLOWLIB. ORG: A distributed materials properties repository from high-throughput ab initio calculations. *Comp Mat Sci* **58**, 227-235 (2012).

48 Jain, A. *et al.* Commentary: The Materials Project: A materials genome approach to accelerating materials innovation. *APL Mater* **1**, 011002 (2013).

49 Kirklin, S. *et al.* The Open Quantum Materials Database (OQMD): assessing the accuracy of DFT formation energies. *npj Comp Mat* **1**, 15010 (2015).

50 Kresse, G. & Furthmüller, J. Efficient iterative schemes for ab initio total-energy calculations using a plane-wave basis set. *Phys Rev B* **54**, 11169 (1996).

51 Kresse, G. & Furthmüller, J. Efficiency of ab-initio total energy calculations for metals and semiconductors using a plane-wave basis set. *Comp Mat Sci* **6**, 15-50 (1996).

52 Choudhary, K., Kalish, I., Beams, R. & Tavazza, F. High-throughput Identification and Characterization of Two-dimensional Materials using Density functional theory. *Scientific Reports* **7**, 5179 (2017).

53 Cao, G. *et al.* Rhombohedral Sb_2Se_3 as an intrinsic topological insulator due to strong van der Waals interlayer coupling. *Phys Rev B* **97**, 075147 (2018).

54 Mostofi, A. A. *et al.* wannier90: A tool for obtaining maximally-localised Wannier functions. *Comp Phys Comm* **178**, 685-699 (2008).

55 Wu, Q., Zhang, S., Song, H.-F., Troyer, M. & Soluyanov, A. A. WannierTools: An open-source software package for novel topological materials. *Comp Phys Comm* **224**, 405-416 (2018).

56 Liu, J. & Vanderbilt, D. Spin-orbit spillage as a measure of band inversion in insulators. *Phys Rev B* **90**, 125133 (2014).

57 Marzari, N. & Vanderbilt, D. Maximally localized generalized Wannier functions for composite energy bands. *Phys Rev B* **56**, 12847 (1997).

58 Souza, I., Marzari, N. & Vanderbilt, D. Maximally localized Wannier functions for entangled energy bands. *Phys Rev B* **65**, 035109 (2001).

59 Please note commercial software is identified to specify procedures. Such identification does not imply recommendation by National Institute of Standards and Technology (NIST).

Supplementary information: High-throughput search for magnetic topological materials using spin-orbit spillage, machine-learning and experiments

Kamal Choudhary^{1,2}, Kevin F. Garrity¹, Nirmal J. Ghimire^{3,4}, Naveen Anand⁵, Francesca Tavazza¹

1 Materials Science and Engineering Division, National Institute of Standards and Technology, Gaithersburg, MD, 20899, USA.

2 Theiss Research, La Jolla, CA 92037, USA.

3. Department of Physics and Astronomy, George Mason University, Fairfax, VA 22030, USA.

4. Quantum Science and Engineering Center, George Mason University, Fairfax, VA 22030, USA.

5. Materials Science Division, Argonne National Laboratory, Argonne, Illinois 60439, USA.

Table S1 Bandgap comparison for PBE+SOC and SCAN+SOC functionals with 1000/atom k-point settings.

JID	PBE+SOC(eV)	SCAN+SOC(eV)
JVASP-44705	0.02	1.2337
JVASP-2817	0.37	1.3048
JVASP-12648	0.27	1.1202
JVASP-10484	0.13	0.9678
JVASP-57388	0.14	0.91
JVASP-16408	0.28	0.5995
JVASP-55805	0.09	0.35
JVASP-21389	0.21	0.4312
JVASP-42538	0.03	0.2225
JVASP-8385	0.2	0.3273
JVASP-44991	0.04	0.116
JVASP-49890	0.01	0.072
JVASP-43466	0.03	0.0865
JVASP-82132	0.03	0.0528
JVASP-26528	0.35	0.3722
JVASP-81597	0.53	0.5518
JVASP-8384	0.01	0.0266
JVASP-16409	0.3	0.3104
JVASP-52135	0	0.0046

JVASP-59757	0	0
JVASP-17989	0	0
JVASP-43095	0	0
JVASP-17898	0	0
JVASP-16012	0	0
JVASP-59630	0	0
JVASP-55644	0	0
JVASP-8538	0	0
JVASP-59509	0	0
JVASP-26231	0	0
JVASP-39287	0	0
JVASP-26527	0	0
JVASP-38244	0	0
JVASP-38246	0	0
JVASP-38201	0	0
JVASP-38157	0	0
JVASP-38248	0	0
JVASP-17268	0	0
JVASP-37701	0	0
JVASP-45925	0	0
JVASP-34486	0	0
JVASP-81304	0	0
JVASP-76959	0	0
JVASP-80606	0	0
JVASP-81275	0	0
JVASP-81033	0.01	0
JVASP-76869	0.06	0.048
JVASP-80151	0.03	0.0142
JVASP-24841	0.04	0.0205
JVASP-16201	0.02	0
JVASP-18368	0.02	0
JVASP-44742	0.02	0
JVASP-76813	0.02	0
JVASP-77062	0.17	0.1493
JVASP-50689	0.03	0
JVASP-17265	0.39	0.3555
JVASP-79685	0.29	0.2462
JVASP-22442	0.16	0.1138
JVASP-81240	0.15	0.103
JVASP-8122	0.11	0.056
JVASP-21125	0.2	0.1449
JVASP-76930	0.16	0.1028
JVASP-21502	0.06	0

JVASP-26681	0.18	0.1136
JVASP-21417	0.07	0

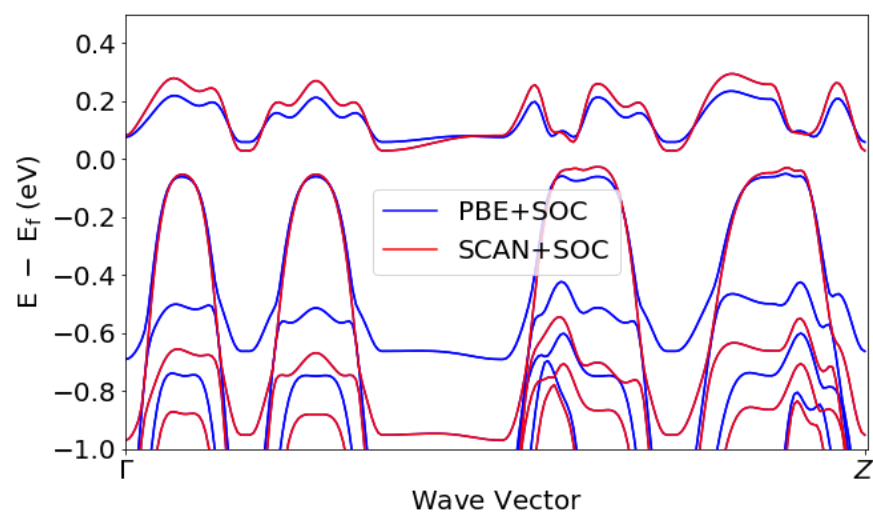


Fig. S1 PBE+SOC and SCAN+SOC bandstructures for NaRuO₂.

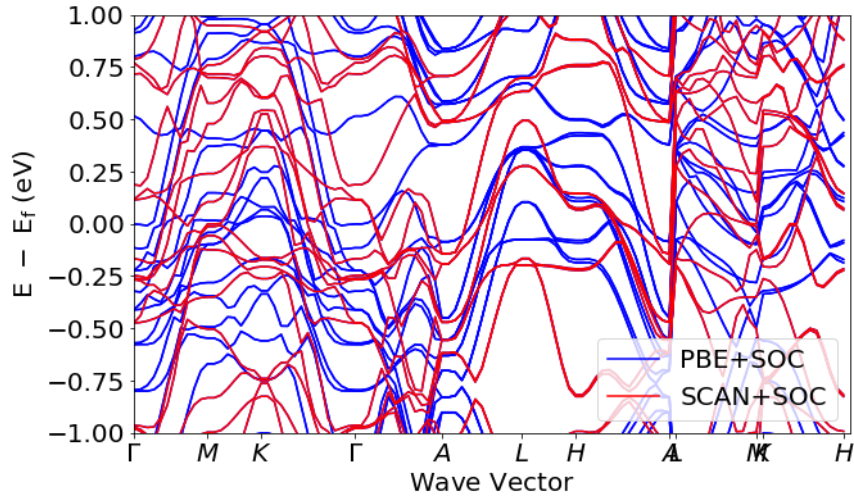


Fig. S2 PBE+SOC and SCAN+SOC bandstructures for Y_3Sn .

Table S2 High-spillage material candidates.

JID	Formula	Spillage	Gap	Magmom	Ehull
JVASP-53555	MnIn_2Te_4	0.828	0	4.963	0
JVASP-53226	Ca_5MnPb_3	7.203	0	9.001	0
JVASP-15074	YCo_5	0.376	0	6.796	0
JVASP-14699	MnTe	1.038	0	8.073	0.012265
JVASP-60253	UTe_3	3.323	0	4.89	0
JVASP-84812	RbMnAs	0.44	0	3.772	0
JVASP-53303	MnTe	0.293	0	13.39	0.061846
JVASP-43433	$\text{Li}_2\text{NbFe}_3\text{O}_8$	2.936	0	3	0
JVASP-60477	RuCl_3	0.264	0	1.985	0
JVASP-43643	$\text{Li}_2\text{CoSnO}_4$	0.322	0	2.789	0.003284
JVASP-43846	MnP_2WO_8	1.539	0	6	0
JVASP-16176	Li_2NbF_6	0.432	0	1	0
JVASP-18583	TiAgHg_2	1.104	0	1.649	0.234241
JVASP-18620	Mn_2Au_5	0.282	0	8.357	0.0225
JVASP-48582	$\text{Li}_6\text{Mn}_5\text{SbO}_2$	5.953	0	21.945	0
JVASP-49957	Li_2RhO_3	0.459	0	1.826	0
JVASP-14962	PuFe_2	4.719	0	3.591	0
JVASP-84911	RbMnAs	0.367	0	3.967	0
JVASP-18519	SrMnBi_2	1.428	0	7.883	0
JVASP-18467	K_2MoCl_6	0.263	0	2	0

JVASP-18551	RbMnSe2	0.302	0	4	0
JVASP-18468	K2OsBr6	0.934	0	1.994	0
JVASP-14964	Mn3Rh	0.815	0	0.903	0.059416
JVASP-14584	CrPt3	2.521	0	2.791	0
JVASP-15006	CrSb2	0.545	0	4.192	0.205306
JVASP-44114	Li2V3SnO8	1.008	0	0.988	0.038036
JVASP-43542	Li3YNi2O6	2.944	0	1.998	0
JVASP-15562	RbFeS2	0.278	0	3.13	0
JVASP-48117	Li2Fe3TeO8	3.823	0	2.025	0.003622
JVASP-60294	UIN	1.201	0.03	4	0
JVASP-43107	Li2Fe3SnO8	0.252	0	4	0.031039
JVASP-14926	VSb	1.02	0	2.891	0.123297
JVASP-20094	Co3Mo	1.016	0	0.9	0
JVASP-54386	NbFeO4	0.523	0	2.015	0
JVASP-18625	VAu2	2.102	0	3.782	0.022372
JVASP-15649	MnCuSb	1.015	0	4.296	0.187604
JVASP-14711	FeAs	0.919	0	1.923	0.002932
JVASP-14928	MnNbSi	1.02	0	2.14	0
JVASP-11974	NbCo3	1.094	0	11.578	0.078038
JVASP-87133	UTe2	2.541	0	4.916	0
JVASP-43362	Li2Fe3TeO8	0.469	0	9.606	0
JVASP-15567	MnCo2Sb	0.304	0	5.793	0.041562
JVASP-43661	Li4Mn3Co3Sn2O6	4.974	0	8.016	0
JVASP-15104	Mn3ZnC	0.551	0	6.801	0.009448
JVASP-15237	HfGaCo2	4.98	0	0.876	0
JVASP-42681	Ti2Co3Te3O6	3.082	0	9.495	0
JVASP-19910	CoPt	1.378	0	4.447	0
JVASP-14889	RuF3	1.989	0	1.975	0
JVASP-50360	Bi2PO6	0.329	0	0.737	0
JVASP-52375	HfMn6Sn6	0.391	0	13.037	0.009234
JVASP-54439	FeB2W2	0.645	0	3.35	0
JVASP-43466	Li2Fe3SbO8	5.063	0.03	3	0.012412
JVASP-18924	FePt3	1.348	0	4.197	0
JVASP-21561	Nb4CrS8	1.024	0	4.931	0
JVASP-14934	CrCuSe2	0.296	0	3	0.254504
JVASP-43125	Cr3SbP4O6	3.53	0.12	9	0
JVASP-42156	Li4Fe3SbO8	2.151	0	8.995	0
JVASP-48191	Li2P2WO8	1.162	0	4	0.007233
JVASP-50895	PrTlO3	0.721	0	2	0
JVASP-18525	Rb2WBr6	0.569	0	2	0
JVASP-52305	Ga2CuO4	0.393	0	1.989	0
JVASP-16908	TiBi2O6	1.081	0	1.891	0.252842
JVASP-16201	MgRhF6	0.902	0.02	0.991	0

JVASP-53381	Cr4Cu3Se8	0.629	0	11.097	0.037619
JVASP-53248	Co2B6W2	0.537	0	17.019	0
JVASP-47467	TaFeO4	0.69	0	2	0.016797
JVASP-19524	UI3	2.823	0.04	6	0
JVASP-50977	Li2CuBiO4	0.594	0	0.723	0
JVASP-15326	CaMn2Sb2	0.517	0	7.131	0
JVASP-16161	ScFeGe	0.446	0	4.543	0
JVASP-42352	HfCrO4	2.027	0	8	0
JVASP-15617	SrCo2P2	0.266	0	0.591	0
JVASP-53515	Mn2SbTe	0.333	0	15.725	0.298565
JVASP-16001	K2RhF6	1.338	0.13	0.994	0
JVASP-6145	US3	1.769	0	4	0
JVASP-60459	UTe3	1.707	0	3.409	0
JVASP-18528	Tl2WCl6	1.043	0	2	0
JVASP-53265	AlFe2Mo	0.389	0	0.789	0
JVASP-50093	TiNbO4	0.654	0	0.533	0
JVASP-43389	Li4MnW3O2	1.119	0.42	4.99	0
JVASP-52989	Sr3Mn4O2	0.462	0	9.994	0
JVASP-43935	Li4Mn3V3Sn2O6	2.408	0	14.756	0
JVASP-43390	Li4Cr5SbO2	7.516	0	3	0
JVASP-43694	CdFeO3	0.395	0	12.87	0
JVASP-15511	FeAgS2	0.276	0	2.056	0.054059
JVASP-726	CrS2	0.308	0	2.047	0
JVASP-14679	VPt3	1.294	0	1.357	0.014238
JVASP-19895	CoPt3	1.687	0	2.833	0
JVASP-15663	MnSbAu	0.904	0	4.559	0.151837
JVASP-53544	Cr4Cu3Te8	1.05	0	11.359	0
JVASP-47523	Co3SbO8	0.28	0	3.696	0
JVASP-42538	Ta2CrNO5	2.788	0.03	6	0
JVASP-6097	VCl3	0.973	0	4	0
JVASP-50922	CuAuO2	0.456	0	0.51	0.012338
JVASP-20076	FeSe	0.421	0	4.509	0.198073
JVASP-18532	CaMn2Bi2	1.171	0	8.652	0.264587
JVASP-49890	Ba4IrO6	2.44	0.01	1.651	0
JVASP-43616	LiFeSbO4	0.354	0	8.13	0.052363
JVASP-51442	GaFe2Co	0.735	0	5.679	0.07515
JVASP-15583	MnAlAu2	0.289	0	3.785	0
JVASP-20110	MnPt3	2.412	0	4.245	0
JVASP-6766	HfFeCl6	1.042	0.02	4	0
JVASP-15211	FeSiRu2	0.394	0	3.686	0
JVASP-50689	Li4Ti3Cu3Te2O6	1.026	0.03	2.771	0
JVASP-1867	FeAgO2	0.75	0	1.032	0.000927
JVASP-16213	MnNbGe	0.381	0	3.711	0

JVASP-14419	CoI2	0.852	0	2.409	0
JVASP-13600	ZrFeCl6	1.015	0.03	4	0
JVASP-57304	Sr3Fe2Cu2Se2O5	1.014	0	7.634	0
JVASP-19831	MnSb	1.005	0	6.273	0.0527
JVASP-56996	TaFe2	2.098	0	2.382	0
JVASP-58164	Mg2TilrO6	2.476	0	1.21	0
JVASP-56764	Tl4CrI6	0.295	0	8	0.00395
JVASP-58491	V4ZnS8	1.181	0	1.181	0
JVASP-57228	Sr2Mn3Bi2O2	0.516	0	11.681	0
JVASP-57886	BaCr4O8	0.354	0	9.992	0
JVASP-56321	RbTiBr3	0.347	0	2.621	0
JVASP-15423	TlCrTe2	0.401	0	3.054	0
JVASP-49947	Na2IrO3	1.294	0	1.798	0
JVASP-57036	Sr2CoCl2O2	0.421	0	2.108	0
JVASP-58165	Ca2TilrO6	2.291	0	0.82	0
JVASP-57153	FeBiO3	0.322	0	2.811	0.100464
JVASP-54622	GaFe2Ni	0.255	0	4.509	0.08455
JVASP-15424	MnRh2Pb	0.881	0	4.674	0
JVASP-51466	NiRh2O4	0.359	0	3.986	8.42E-05
JVASP-58166	TiZn2IrO6	1.96	0	1.126	0
JVASP-35684	Mn3Sn	0.477	0	1.01	0.216904
JVASP-58167	Mg2SnIrO6	1.657	0	0.865	0
JVASP-21107	Mn3P6Pd2O	1.106	0	14.047	0
JVASP-57905	BaTi4O7	0.408	0	3.473	0.119577
JVASP-15256	FeCuPt2	1.662	0	3.93	0
JVASP-54890	RbW3Cl9	0.579	0.06	1.616	0
JVASP-58177	Mg2MnIrO6	1.523	0	4.194	0
JVASP-59902	ZnCr2S4	0.303	0	12	0.158825
JVASP-58503	ZnFe4S8	1.05	0	6.979	0
JVASP-35299	MnCoSn	1.013	0	8.783	0.348821
JVASP-59607	YMnGe	0.411	0	11.184	0
JVASP-58179	Mg2ColrO6	1.673	0	2.154	0
JVASP-15693	Mn2Sb	0.5	0	11.488	0.333028
JVASP-15730	ThCo2Si2	1.149	0	0.97	0
JVASP-51048	FeCu2SnS4	0.313	0	3.874	0.006128
JVASP-15428	KCo2Se2	1.006	0	2.002	0
JVASP-56922	MnAsRh	0.347	0	9.719	0
JVASP-51894	FeBiO3	2.269	0	13.908	0.005442
JVASP-57388	MnBiAsO5	3.258	0.14	10	0
JVASP-57951	YCu3Sn4O2	1.146	0	2.015	0
JVASP-58180	Zn2ColrO6	1.813	0	1.382	0
JVASP-54898	SrCo2As2	0.471	0	0.846	0
JVASP-16042	TaF3	0.497	0	1.99	0.448904

JVASP-18575	Rb ₂ WC ₁₆	0.591	0	2	0
JVASP-58507	Ca ₂ CuIrO ₆	2.84	0	3.717	0
JVASP-49616	ZnFeO ₃	0.9	0	8.717	0.063702
JVASP-57848	Ba ₆ Ru ₃ Cl ₂ O ₂	0.513	0	3.365	0
JVASP-55136	Fe ₃ PtN	1.033	0	7.954	0
JVASP-57242	Sr ₂ Fe ₂ S ₂ O ₂ F ₂	0.472	0	7.526	0
JVASP-59737	Ta ₂ CuO ₆	0.354	0	1.997	0
JVASP-21401	NaSr ₃ IrO ₆	3.184	0.23	3.893	0
JVASP-54949	Co ₂ Sn	1.118	0	2.772	0.219942
JVASP-19286	Y ₂ Fe ₂ O ₇	3.858	0	8.012	0
JVASP-57319	Ba ₂ YFe ₃ O ₈	0.506	0	4.796	0
JVASP-8616	Sr ₂ CoBr ₂ O ₂	0.282	0	2.128	0
JVASP-55156	Fe ₃ RhN	1.011	0	8.232	0
JVASP-59673	Y ₂ Ru ₂ O ₇	2.262	0	1.468	0
JVASP-57430	Ba ₂ Mn ₂ Bi ₂ O	2.292	0	19.266	0
JVASP-15076	FePd	0.28	0	6.495	0.024811
JVASP-15057	Fe ₃ Se ₄	0.506	0	4.125	0.079199
JVASP-60098	YFeO ₃	0.805	0	24.747	0.037703
JVASP-8096	Cr ₂ FeSe ₄	0.613	0	5.997	0
JVASP-58040	Ba ₂ TiFe ₂ O ₇	1.942	0	7.098	0
JVASP-54955	KMnAg ₃ C ₆ N ₆	1.008	0	1	0.166123
JVASP-14753	HfZn ₂	1.052	0	1.177	0.002744
JVASP-55644	KFeBr ₃	0.339	0	16	0
JVASP-38339	RbAuO ₃	1.701	0	1.329	0.414073
JVASP-58042	Ba ₂ TiCo ₂ O ₇	0.317	0	5.352	0
JVASP-8618	CrPbO ₃	1.021	0	2	0
JVASP-5314	UCl ₅	1.152	0.41	2	0
JVASP-59564	V ₂ CdO ₄	1.025	0	8	0
JVASP-58337	KY ₂ Ti ₂ S ₂ O ₅	0.326	0	0.917	0
JVASP-59847	YMn ₃ Se ₂ ClO ₈	0.419	0	18.612	0
JVASP-60099	YCoO ₃	1.365	0	11.449	0.139314
JVASP-36101	Er ₂ Co ₃ Ge ₅	1.248	0	0.916	0
JVASP-57577	TiFeBi ₂ O ₆	0.284	0	4.001	0
JVASP-56803	Ba ₃ Fe ₃ Se ₇	0.484	0	19.803	0
JVASP-8619	SrCrO ₃	0.639	0	1.973	0
JVASP-57326	Ni ₂ Ag ₃ O ₄	1.039	0	2.738	0.02373
JVASP-56962	CrGaCo ₂	1.008	0	3.035	0
JVASP-58227	BaMgCo ₄ O ₈	0.411	0	11.524	0
JVASP-7958	MnAsRh	0.32	0	8.557	0.087241
JVASP-59570	Ba ₃ Cr ₂ O ₈	0.409	0	2	0
JVASP-8018	MnIr	2.046	0	2.495	0
JVASP-37845	CuSeO ₄	0.455	0	1.95	6.24E-05
JVASP-58095	YCoO ₃	1.009	0	3.761	0.163071

JVASP-7892	BaY2NiO5	1.009	0	1.252	0
JVASP-57868	CrSn2	0.29	0	1.647	0.181985
JVASP-60101	YMoO3	0.837	0	10.18	0.053661
JVASP-12919	CuPtF6	0.631	0	1.999	0
JVASP-59682	RbHgN3O6	1.012	0	4	0.343516
JVASP-56072	MnBi	2.039	0	6.924	0.277582
JVASP-21191	Ca2NilrO6	1.31	0	1.549	0
JVASP-59496	Cd2Re2O7	2.491	0	1.746	0
JVASP-42985	Li5Nb2V5O2	1.047	0	3.417	0
JVASP-59573	Sr3NilrO6	2.902	0	4.471	0
JVASP-59637	Mn4Ge6Ir7	1.728	0	16.86	0
JVASP-41091	Ta2FeOs	0.945	0	1.545	0
JVASP-55190	Rb2FeI4	0.373	0	8	0.000214
JVASP-60102	YVO3	1.014	0	10.626	0.087396
JVASP-8623	FeBiO3	0.323	0	3.258	0.041491
JVASP-56304	TlCoCl3	1.032	0	5.985	0
JVASP-21588	Sr2SclrO6	3.617	0	3.152	0
JVASP-58461	BaFe4O8	0.266	0	10.253	0
JVASP-2817	K4IrO4	0.632	0.37	2.88	0
JVASP-14308	Ta2InCuTe4	0.508	0	2.969	0.336609
JVASP-13174	Ta2CrO6	0.451	0	7.356	0
JVASP-56818	MnSbPt	0.854	0	3.913	0.372015
JVASP-59580	BaVO3	0.653	0	1.154	0
JVASP-49659	Nb2Co2O9	1.003	0	3.882	0.15346
JVASP-8538	CeNiSb2	2.223	0	0.546	0
JVASP-58250	YCo4B	0.544	0	6.681	0
JVASP-59704	Fe2CuGe2	0.393	0	0.508	0
JVASP-59773	Mn3GeIr	0.859	0	38.663	0.138852
JVASP-54797	CrCoPt2	1.687	0	1.199	0
JVASP-58411	Rb2CoSe2	1.034	0	5.996	0
JVASP-59709	In2CoS4	0.547	0	5.991	0
JVASP-55805	LiMnAsO4	8.433	0.09	20	0
JVASP-59509	Ta3Co3C	1.468	0	4.005	0
JVASP-59587	YMnO3	1.006	0	7.998	0
JVASP-8240	YFeO3	0.618	0	2.557	0.197367
JVASP-41131	Hf2CoIr	1.023	0	0.69	0
JVASP-59648	Mn3Silr	2.239	0	25.834	0.052054
JVASP-21327	Zn2BiWO6	1.488	0	1.15	0
JVASP-20932	Cr2CuSe4	0.45	0	10.336	0
JVASP-58257	FeRh2S4	1.214	0	6.105	0
JVASP-7856	YCrO3	1.228	0	2.978	0.144098
JVASP-59882	YCo2S4	3.012	0	1.785	0.142833
JVASP-21582	MnNb3S6	1.016	0	8.337	0

JVASP-57296	SrFe2Se4O2	1.933	0	5.999	0
JVASP-8323	CoBi2O6	2.093	0	1.784	0.180329
JVASP-59593	NiRh2O4	0.322	0	3.986	0
JVASP-20447	FePt	0.413	0	3.243	0
JVASP-38273	KRhO3	0.349	0	1.784	0
JVASP-21693	HfMn2	2.318	0	2.938	0
JVASP-45533	YFeO3	1.32	0	11.999	0
JVASP-7858	TlFeO2	1.084	0	5.29	0
JVASP-21125	Sr3LiIrO6	4.647	0.2	3.869	0
JVASP-21071	Cr2HgSe4	1.029	0	11.956	0
JVASP-20414	Co3W	0.255	0	0.833	0.096612
JVASP-26876	CeH2	0.973	0	0.763	0
JVASP-38639	Ni3Au	1.081	0	1.538	0.088389
JVASP-21589	Ba2SclrO6	2.197	0	3.073	0
JVASP-59107	Zr6Co23	0.415	0	25.261	0
JVASP-41448	TmUTc2	2.133	0	0.877	0
JVASP-20397	ZrMn2	0.264	0	2.878	0.000832
JVASP-8633	VPbO3	0.328	0	1	0
JVASP-8737	MnPd3	0.372	0	9.241	0
JVASP-26681	Na3OsO5	1.26	0.18	2.702	0
JVASP-8433	BaMnGe	0.329	0	7.109	0
JVASP-12965	Mn3As2	0.392	0	14.986	0.095392
JVASP-26231	Co2B6Mo2	0.444	0	17.539	0
JVASP-20780	Rb2O3	0.942	0	4	0
JVASP-8249	YCrO3	1.23	0	2.978	0.143851
JVASP-39263	FeAg3	0.397	0	2.97	0.356336
JVASP-24357	Sr3CalrO6	2.334	0	1.645	0
JVASP-41360	HfScCo2	1.189	0	0.652	0
JVASP-22381	Sr4IrO6	2.288	0	1.604	0
JVASP-22441	Na3Cd2IrO6	1.503	0.23	1.831	0
JVASP-22442	Ba3NaIrO6	1.853	0.16	3.946	0
JVASP-49567	MgMo6O6	2.044	0	2.361	0
JVASP-39364	Ni3Hg	1.068	0	0.883	0.285456
JVASP-25704	NbVF6	0.466	0	4	0
JVASP-15904	MnSbIr	1.029	0	3.103	0
JVASP-8204	NiPt	2.669	0	1.828	2.00E-05
JVASP-26047	Co2Re2B6	0.768	0	17.729	0
JVASP-8335	ZnCr2N2	0.288	0	5.855	0.382623
JVASP-39275	FeAu3	0.315	0	3.117	0.168094
JVASP-8122	NaRuO2	0.496	0.11	1	0.021784
JVASP-26796	Li2MoF6	1.034	0	4	0
JVASP-7922	BaMn2P2	0.342	0	2.791	0
JVASP-7868	FeAgO2	0.766	0	2.083	0

JVASP-38211	Rb3Pb	1.125	0	0.912	0
JVASP-38310	RbInO3	0.298	0	2	0.284021
JVASP-39279	FePbO3	0.298	0	3.441	0
JVASP-7869	Sr2MnO4	0.283	0	3	0
JVASP-26074	Rb3Fe2Se4	1.094	0	30.015	0
JVASP-16563	MnSnIr	0.672	0	3.447	0.344516
JVASP-7702	TiAu	1.023	0	0.934	0.113969
JVASP-38264	MnTl3	1.228	0	8.367	0.456432
JVASP-38317	RbF3	0.411	0	2	0.161013
JVASP-20801	Cr2Te3	1.454	0	24.218	0
JVASP-21389	Sr3CuPtO6	2.174	0.21	1.919	0
JVASP-14273	TiCdHg2	0.529	0	0.835	0.175958
JVASP-15949	ZnFe3C	0.295	0	4.078	0
JVASP-38319	RbMnO3	0.387	0	1.908	0
JVASP-22401	Sr3MnN3	1.01	0	2.486	0
JVASP-38492	K3Rh	1.073	0	0.501	0.477367
JVASP-19159	YFe4Cu3O2	0.819	0	9.021	0
JVASP-15951	ZnCo3C	1.005	0	0.927	0
JVASP-8510	Cr2As	0.86	0	3.255	0.162059
JVASP-39287	K3Sn	0.424	0	0.912	0
JVASP-38226	MnSn3	0.302	0	7.979	0.339145
JVASP-21417	Sr3ZnIrO6	2.193	0.07	1.436	0
JVASP-38325	RbNiO3	0.383	0	2.666	0
JVASP-26526	Ba2Fe2S2OF2	0.314	0	7.827	0
JVASP-8301	MgMoF6	1.013	0	2	0
JVASP-15918	LiTiTe2	1.022	0	0.843	0
JVASP-26527	SrCrF6	0.284	0	2	0
JVASP-21422	Ba2CaOsO6	0.603	0	1.822	0
JVASP-38183	Rb3Tl	1.317	0	1.175	0.035357
JVASP-8567	Li2FeBr4	0.852	0	4	0
JVASP-8609	Sr2CoCl2O2	0.414	0	2.115	0.000768
JVASP-16654	CoCu2SnSe4	0.616	0	2.458	0
JVASP-26528	Rb2IrF6	1.404	0.35	0.996	0
JVASP-27213	Ni2Hg2OF6	1.058	0	8.165	0
JVASP-37387	Th3U	2.582	0	2.336	0.250054
JVASP-15391	TlCo2Se2	0.426	0	1.794	0
JVASP-16407	LiRhF6	0.561	0	1.999	0
JVASP-21502	Li2RhF6	2.022	0.06	1.993	0
JVASP-16367	MnAlPt	1.054	0	6.85	0
JVASP-27661	Zn2Fe3O8	0.465	0	12	0
JVASP-38614	MgPbO3	0.391	0	2	0.092507
JVASP-16368	MnAlPt2	1.057	0	4.176	0
JVASP-38289	RbSrO3	0.331	0	3	0

JVASP-16408	LiIrF6	1.158	0.28	2	0
JVASP-26823	Ba3NiIr2O9	3.343	0	9.097	0
JVASP-19598	V3Te4	0.92	0	6.915	0.008259
JVASP-16409	K2IrF6	1.396	0.3	0.995	0
JVASP-22415	Sr3MgIrO6	1.99	0.12	1.588	0
JVASP-16823	CrTe4Au	0.542	0	2.872	0
JVASP-14403	Mn2Sb	0.5	0	11.488	0.333028
JVASP-38341	RbAgO3	1.28	0	1.663	0.39356
JVASP-8383	YWF5	1.5	0	3.498	0
JVASP-17460	Ba2Mn3As2O2	3.292	0	3.371	0
JVASP-858	Co	0.531	0	3.153	5.10E-06
JVASP-55303	Mn3TeO6	0.305	0	29.848	0.054318
JVASP-17641	CaMnGe	0.313	0	4.563	0
JVASP-55470	Co2Mo3O8	7.451	0	0.623	0
JVASP-19739	TiHg	1.407	0	1.372	0.148755
JVASP-17315	CrAsRh	0.259	0	10.625	0.000782
JVASP-8384	YNiF5	0.372	0.01	2	0
JVASP-38244	Rb3In	0.418	0	1.284	0.094258
JVASP-39452	RuAu3	1.302	0	1.719	0.368509
JVASP-17265	BaIrF6	1.356	0.39	0.997	0
JVASP-17509	RhO2F6	3.993	0	4.048	4.00E-06
JVASP-8349	ZnCoF6	0.321	0	1	0
JVASP-19704	NbF4	0.254	0	0.682	0
JVASP-17643	CoNiSn	1.014	0	1.788	0.007715
JVASP-39453	RuAu3	1.487	0	3.489	0.397432
JVASP-38515	KAgO3	0.91	0	1.549	0.394317
JVASP-37981	CoTeO3	0.544	0	0.729	0.307307
JVASP-16338	FeTe	0.654	0	3.87	0.207063
JVASP-37453	TaTiFe2	1.042	0	0.83	0
JVASP-8385	YCoF5	1.175	0.2	3	0
JVASP-12407	TiFe6Ge6	1.016	0	8.704	0
JVASP-38248	Rb3Ga	0.469	0	1.472	0.112694
JVASP-17730	FeSn	1.009	0	3.584	0.176643
JVASP-16719	YFe2B2	0.429	0	1.027	0
JVASP-47356	Li2Si2WO7	0.887	0	4	0
JVASP-12287	ZrMnGe	0.267	0	8.375	0
JVASP-12608	Sr3Co2Cl2O5	0.693	0	3.49	0
JVASP-17854	Mn3SnC	0.392	0	3.33	0.009175
JVASP-17646	RbMnAs	0.255	0	3.881	0
JVASP-37314	SrAlO3	2.995	0	0.526	0
JVASP-36857	MnAuO2	0.374	0	3.984	0
JVASP-46728	Li4Mn3SbP4O6	3.224	0.09	15.761	0
JVASP-21188	Ca2FeIrO6	0.982	0	5.586	0

JVASP-17462	Sr2Mn3As2O2	3.371	0	7.453	0
JVASP-18123	FePd3	0.402	0	4.169	0
JVASP-19789	CrSb	0.378	0	5.604	0.153325
JVASP-17168	MoPt3	1.132	0	1.472	0.15261
JVASP-37028	TiInFe2	2.041	0	0.907	0
JVASP-16723	CrIr3	1.093	0	1.237	0
JVASP-10854	YFe2O4	0.834	0	14	0.213896
JVASP-37407	TePdO3	0.99	0	1.019	0
JVASP-37144	NbFe3	1.008	0	5.132	0
JVASP-49613	Y2Co2O7	0.266	0	1.903	0
JVASP-44414	Li2Mn3WO8	1.054	0	16.292	0
JVASP-46240	CoBi2O6	4.185	0	0.549	0
JVASP-12612	Ba2UCoO6	1.058	0	3.011	0
JVASP-18049	CeB6	0.88	0	0.721	0
JVASP-15970	Cr3SnN	1.006	0	1.687	0
JVASP-16474	TiCdHg2	0.529	0	0.835	0.175958
JVASP-44705	MnSb4O2	1.432	0.02	3	0
JVASP-10855	ZnFe2O4	3.993	0	4.001	5.50E-05
JVASP-37189	Mn3Ga	0.754	0	3.11	0.095038
JVASP-11508	TiBi2O6	1.145	0	3.857	0.332215
JVASP-11584	Sr4MgFe2S2O6	0.343	0	8.37	0
JVASP-37701	Y3Sn	0.286	0	1.596	0.106332
JVASP-8357	AlWF5	1.143	0	3.97	0
JVASP-8414	BaYCoCuO5	0.557	0	2.252	0
JVASP-49615	YMoO3	0.705	0	3.257	0.001451
JVASP-44418	Na3CrBAsO7	6.077	1.09	6	0
JVASP-17654	MnGaPt	0.463	0	3.336	0.246664
JVASP-37190	MnGaFeCo	1.018	0	3.068	0
JVASP-17478	Sc3In	1.013	0	2.465	0
JVASP-45802	Li8Cr3TeO2	3.222	0	5.932	0
JVASP-27678	Mn4ZnCu3O2	1.061	0	9.079	0
JVASP-18328	NaMnBi	0.348	0	8.108	0.057047
JVASP-11811	Ba2Mn2Sb2O	0.444	0	19.229	0
JVASP-18131	FeCu2Sn	0.881	0	2.688	0.263135
JVASP-12355	Zr2Fe3Ge	0.336	0	7.794	0
JVASP-38645	Ni3Au	1.248	0	3.103	0.097749
JVASP-11692	RbFeMo2O8	0.7	0	1	0
JVASP-37208	SiPdO3	1.016	0	1.954	0
JVASP-44507	Li2MnBAsO7	2.041	1.17	6	0
JVASP-10857	ZnCr2Se4	1.012	0	11.98	0
JVASP-17618	Mn2GaCo	2.034	0	2.019	0
JVASP-37946	Co3Bi	1.067	0	2.899	0.443311
JVASP-18209	Mn3Sn	0.789	0	10.047	0.202535

JVASP-18104	VCu2Sn	0.411	0	2.813	0
JVASP-17328	Mn3ZnN	1.005	0	4.201	0
JVASP-38764	ZnFeRh2	0.52	0	4.221	0
JVASP-52119	MnReO4	2.649	0	7.645	1.75E-06
JVASP-17828	ZnFeSb	0.582	0	2.538	0.474698
JVASP-18136	NdCoSi	0.936	0	0.511	0
JVASP-37600	Sr3Cr	1.006	0	4.864	0.495398
JVASP-8416	BaYVCuO5	3.021	0	1.571	0
JVASP-44720	P2WO7	2.354	0	4	0.008388
JVASP-37040	TiAu	1.722	0	1.708	0.04604
JVASP-18366	K2RuCl6	1.011	0	2	0
JVASP-42952	Li4Co3TeO8	0.945	0	9.012	0
JVASP-19792	Fe3Pt	1.068	0	8.229	0.057277
JVASP-46260	Li2Ni3BiO8	2.085	0	2.988	0
JVASP-37424	Ta2Be2O5	1.309	0	0.702	0
JVASP-10656	ZnMo2O4	0.664	0	3.853	0.156794
JVASP-36884	TlFeF3	0.305	0	4	0
JVASP-16803	MnAu	0.38	0	4.067	0.121371
JVASP-44512	Li4Mn5NbO2	0.993	0	2.81	0
JVASP-44654	LiZnFeO06	8.443	0	15.74	0
JVASP-16853	Ni3Pt	1.307	0	2.199	0
JVASP-16804	MnAu	1.04	0	4.069	0.121112
JVASP-36885	TlCoF3	0.297	0	3	0
JVASP-17300	BaMn2As2	0.35	0	3.707	0
JVASP-17454	Sr2CoO4	0.271	0	1.953	0
JVASP-18213	MnCu2SnSe4	0.296	0	4.636	0
JVASP-16854	CoCu2Sn	0.4	0	0.955	0.222465
JVASP-17624	PuFe2Si2	2.996	0	4.569	0
JVASP-18302	VGaCo2	0.415	0	1.943	5.55E-05
JVASP-16806	NaMnTe2	1.044	0	4.052	0.093483
JVASP-18368	K2OsCl6	1.079	0.02	1.999	0
JVASP-11590	Sr4CaFe2S2O6	0.482	0	8.477	0
JVASP-37044	TiFe2As	0.274	0	1.008	0
JVASP-45852	Li2Nb2Fe3O0	1.282	0.08	8.067	0
JVASP-17625	Mn3GeC	0.333	0	2.997	0
JVASP-44518	Li5Nb2Fe5O2	5.969	0	15	0.043384
JVASP-18303	MnTePd	0.49	0	4.838	0
JVASP-20640	FePt	0.413	0	3.243	0
JVASP-17790	Mn2Sb	1.03	0	2.746	0.124949
JVASP-17237	FeNiPt2	0.661	0	4.629	0
JVASP-18214	BaMn2Ge2	1.008	0	4.419	0
JVASP-34926	Sr5Bi3	1.492	0	1.639	0
JVASP-17471	Sr2Mn3Sb2O2	3.303	0	8.403	0

JVASP-36950	CaTcO3	0.45	0	1.819	0
JVASP-9317	YFeW2O8	4.021	0	3.593	0
JVASP-18255	InFe2CuSe4	1.021	0	7.611	0
JVASP-46173	HfFeO3	1.518	0	16	0
JVASP-18349	TiI3	0.969	0	0.704	0.003149
JVASP-45854	Li3Nb2Fe3O0	2.947	0	5.002	0.026501
JVASP-17457	Ba2Mn3Sb2O2	1.028	0	9.098	0
JVASP-11697	LiFeAs2O7	0.353	0	4.997	0
JVASP-17394	MnCu2Sb	0.752	0	3.86	0.300664
JVASP-18174	Co2As	1.064	0	4.734	0.27925
JVASP-44438	Li2Co3SnO8	0.326	0	1.631	0
JVASP-17718	Mn2Ge	0.344	0	8.937	0.088172
JVASP-19978	NbF3	0.308	0	2	0.08838
JVASP-37051	Ti2GaFe	0.856	0	0.982	0
JVASP-44593	Li4Mn3Sn5O6	3.986	0	12.94	0
JVASP-19388	Ca2FeSbO6	0.337	0	8.905	0
JVASP-44528	Li2Co3TeO8	1.45	0	0.962	0
JVASP-11093	ZnFe4S8	0.621	0	6.639	0.033962
JVASP-34927	Ba5Bi3	2.017	0	1.848	0
JVASP-11592	Sr4MgCo2S2O6	1.067	0	5.16	0
JVASP-17303	CdRhF6	0.767	0.09	0.992	0
JVASP-17637	MnGaNi2	0.298	0	4.013	0.00848
JVASP-45210	NbV3O8	4.062	0	7.962	0
JVASP-18176	Rb2RhF6	1.013	0.19	0.996	0
JVASP-46361	TaFeO4	2.096	0	4.012	0
JVASP-34315	CuSeO4	0.457	0	1.95	0
JVASP-20585	ZrMn2	0.264	0	2.878	0.000832
JVASP-17721	MnSnPd2	0.25	0	4.136	0
JVASP-9209	Ba2YCo3O7	1.016	0	6.49	0
JVASP-18028	FeTe	0.283	0	4.155	0.104371
JVASP-36838	NiAuO2	0.432	0	1.669	0
JVASP-18220	Mn2CoSn	0.357	0	1.885	0.150639
JVASP-8486	PuNi5	3.485	0	3.303	0
JVASP-12626	InFeO3	0.624	0	5.654	0
JVASP-20602	Co3W	0.255	0	0.833	0.096613
JVASP-17304	HgRhF6	0.701	0	0.981	0
JVASP-44617	Li2Fe3SnO8	0.503	0	4.156	0.085692
JVASP-44742	Li5Ni5Sn2O2	5.359	0.02	8.956	0
JVASP-46857	Li2Co3SnO8	0.27	0	0.859	0.020608
JVASP-44461	VBiO3	0.756	0	8	0.014917
JVASP-19396	Ca2SbMoO6	0.43	0	2.121	0
JVASP-12627	Sr3Fe2Cl2O5	0.288	0	7.522	0
JVASP-18082	MnSnPt	0.399	0	3.63	0

JVASP-17803	FeSb2	0.727	0	1.72	0
JVASP-46861	FeSbO4	0.268	0	5.77	0
JVASP-42911	LiMnSbO4	4.231	0	9.477	0
JVASP-10907	AlBi3O9	0.588	0	5.951	0.027749
JVASP-18193	FeCo2Ge	0.291	0	5.279	0
JVASP-43066	CoSbO4	0.357	0	0.776	0
JVASP-44991	FeSb4O2	2.071	0.04	2	0
JVASP-44750	Li2Ni3WO8	1.136	0	3.997	0
JVASP-34319	TlV3Cr2S8	2.865	0	6.571	0
JVASP-45016	LiFeSnO4	0.456	0	2	0
JVASP-12631	CdFe2O4	1.621	0	4.006	0
JVASP-10484	Ba2SrIrO6	0.824	0.13	2.617	0
JVASP-9343	VW2O8	0.773	0	0.894	0
JVASP-9897	Mg2CrWO6	1.216	0	3.683	0
JVASP-12217	ZnFe2O4	6.588	0	4.001	4.93E-06
JVASP-9466	Ba2TlNi2O7	0.465	0	3.151	0
JVASP-34389	FeSnF6	0.503	0	4.039	0
JVASP-9216	Ba2YNi3O7	0.288	0	0.603	0
JVASP-12231	KFeMo2O8	0.529	0	1	0
JVASP-12637	FeMoClO4	2.006	0	4.497	0
JVASP-11536	YV2O4	0.506	0	9.995	0.094075
JVASP-10731	ZnCo4O8	0.253	0	1.777	0.01025
JVASP-9469	Ba2YTlV2O7	2.984	0	3.127	0
JVASP-9640	YCu2O4	1.012	0	5.939	0.335261
JVASP-9527	VZnSF5	1.25	0	3.998	0
JVASP-9203	Ba2AlNi3O8	1.083	0	1.341	0
JVASP-9676	ZnCr2Se4	1.012	0	11.98	1.06E-05
JVASP-9196	Ba2AlCr3O8	3.056	0	9	0
JVASP-34404	NbCrF6	3.008	0	2.115	0
JVASP-52140	Ba3Ti3O8	0.38	0	1.571	0.016329
JVASP-34347	BaFeF4	0.924	0	8	0
JVASP-9363	BaZnFe4O8	1.021	0	18.898	0
JVASP-11670	Sr2CoMoO6	0.312	0	2.993	0
JVASP-9258	Sr2AlTiV2O7	3.397	0	4	0
JVASP-11731	MnPt3O6	0.276	0	4.87	0
JVASP-9962	V2ZnO4	0.342	0	6.627	0.117976
JVASP-9185	Ba2YV3O8	1.012	0	2.24	0
JVASP-12643	Ba2UMnO6	1.931	0	5	0
JVASP-34878	K2Zr7Cl8	0.894	0	1.885	0
JVASP-34479	Ba4Fe2S4I5	0.512	0	0.957	0
JVASP-10839	YMnO3	1.006	0	7.998	1.11E-05
JVASP-9366	BaCaCo4O8	0.802	0	7.42	0
JVASP-9966	ZnFe2O4	0.529	0	12.329	0.144093

JVASP-34752	KCdN3O6	0.544	0	4.001	0.377445
JVASP-12648	MnSnB2O6	0.926	0.27	5	0
JVASP-34485	ZrCoF6	0.875	0.18	3	0
JVASP-9267	Sr2YTIV2O7	1.041	0	2.878	0
JVASP-24743	Fe3W3N	1.934	0	4.38	0
JVASP-34425	Ba6Ru2PtCl2O2	4.102	0	5.99	0
JVASP-9187	Ba2YCo3O8	1.025	0	2.726	0
JVASP-9269	Ba2TlBi2O7	1.109	0	0.555	0
JVASP-78840	Mn3Ge	3.009	0	1.039	0.000129
JVASP-9491	Sr2FeCuSO3	0.348	0	8.436	0
JVASP-9541	YFeO3	1.005	0	8.072	0.059007
JVASP-34429	ZrFeF6	1.004	0	4	0.013753
JVASP-10342	Ge2MoO6	0.277	0	3.999	0
JVASP-52113	Sr2CoReO6	0.407	0	2.047	0
JVASP-24596	RbCoCl3	0.309	0	5.992	0
JVASP-9494	ZnCoPO5	1.109	0	2.002	0
JVASP-79568	MnGaFe2	1.942	0	2.075	0
JVASP-78684	MnSnPt	0.274	0	3.406	0.210315
JVASP-79239	Mn3Pt	0.791	0	1.908	0.093006
JVASP-9495	Sr2CoSO3	1.033	0	4.155	0
JVASP-79241	MnGePd2	0.428	0	4.112	0
JVASP-79574	NbFe3	0.886	0	3.23	0.06218
JVASP-9931	ZnFe2O4	5.142	0	4.001	0
JVASP-9496	Sr2MnSO3	0.286	0	6.149	0
JVASP-79576	MnGaFe2	0.319	0	6.399	0.037086
JVASP-78859	NiBrO	1.006	0	1.299	0
JVASP-79583	Mn2CuGe	0.438	0	0.669	0.107469
JVASP-79200	VGaCo2	0.4	0	1.943	0
JVASP-24841	Y6OsI0	1.144	0.04	1.177	0
JVASP-80740	Ti2GaFe	0.849	0	0.982	8.37E-05
JVASP-79431	MgMnPt2	1.202	0	4.386	0
JVASP-79586	VFeCoAs	1.004	0	2.944	0
JVASP-16934	YCoO3	1.005	0	1.171	0.25161
JVASP-78508	CoSI	0.685	0	1.969	0.44561
JVASP-78280	Mn2Sb	1.068	0	1	0.143192
JVASP-79206	FeSe	0.421	0	4.509	0.198133
JVASP-79916	NbZnCo2	0.537	0	0.74	0
JVASP-78380	BaN	0.442	0	1	0.268514
JVASP-78429	NaSe	0.252	0	0.915	0.374696
JVASP-79435	Mn2CoSn	0.729	0	1.883	0.150843
JVASP-78470	RbSe	0.288	0	0.998	0.455465
JVASP-78658	NiPt	2.665	0	1.828	0
JVASP-79097	Mg3Re	1.082	0	0.51	0.361552

JVASP-79593	Fe3Pt	1.068	0	8.23	0.057144
JVASP-80098	MnTe	1.038	0	8.073	0.012304
JVASP-78434	KSe	0.252	0	0.996	0.421998
JVASP-79500	VFeCoGe	0.629	0	1.954	0
JVASP-82132	MnBi2Te4	1.368	0.03	4.998	0
JVASP-80251	CrSnRh2	0.297	0	2.89	0.238679
JVASP-78832	MnBi	2.039	0	6.925	0.277638
JVASP-79457	CrInNi2	0.459	0	3.557	0.082176
JVASP-79604	VGaFeCo	0.413	0	0.952	0
JVASP-79562	GaFeNi2	0.339	0	3.035	0.004254